








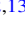





# TESS Photometry of AM Her and AR UMa: Binary Parameters, Cyclotron Emission Modeling, and Mass Transfer Duty Cycles

Paul A. Mason<sup>1,2</sup> , Pasi Hakala<sup>3</sup>, Kinwah Wu<sup>4</sup> , Paul E. Barrett<sup>5</sup> , Krystian Iłkiewicz<sup>6,7</sup> , Colin Littlefield<sup>8</sup> , Lorena C. Monroy<sup>2</sup>, Hasan C. Sezer<sup>2</sup>, Francisco Jablonski<sup>9</sup> , Peter Garnavich<sup>10</sup> , Paula Szkody<sup>11</sup> , Gavin Ramsay<sup>12</sup> , Christopher Duffy<sup>12,13</sup> , and Simone Scaringi<sup>6</sup> 

<sup>1</sup>New Mexico State University, MSC 3DA, Las Cruces, NM 88003, USA; [pmason@nmsu.edu](mailto:pmason@nmsu.edu)

<sup>2</sup>Picture Rocks Observatory, 1025 S. Solano Dr. Suite D., Las Cruces, NM 88001, USA

<sup>3</sup>Finnish Centre for Astronomy with ESO, Quantum, Vesilinnantie 5, FI-20014, University of Turku, Finland

<sup>4</sup>Mullard Space Science Laboratory, University College London, Holmbury St. Mary, Surrey RH5 6NT, UK

<sup>5</sup>Department of Physics, The George Washington University, Washington, DC 20052, USA

<sup>6</sup>Centre for Extragalactic Astronomy, Department of Physics, Durham University, South Road, Durham DH1 3LE, UK

<sup>7</sup>Astronomical Observatory, University of Warsaw, Al. Ujazdowskie 4, 00-478 Warsaw, Poland

<sup>8</sup>Bay Area Environmental Research Institute, Moffett Field, CA 94035, USA

<sup>9</sup>Instituto Nacional de Pesquisas Espaciais, Av. dos Astronautas 1758, São José dos Campos, SP 12227-010, Brazil

<sup>10</sup>Department of Physics, University of Notre Dame, Notre Dame, IN 46556, USA

<sup>11</sup>Department of Astronomy, University of Washington, Seattle, WA 98195, USA

<sup>12</sup>Armagh Observatory and Planetarium, College Hill, Armagh, UK

<sup>13</sup>Department of Physics, University of Warwick, Gibbet Hill Road, Coventry CV4 7AL, UK

Received 2023 October 30; revised 2024 January 16; accepted 2024 February 1; published 2024 April 10

## Abstract

Transiting Exoplanet Survey Satellite (TESS) photometry of the polars AM Herculis (AM Her) and AR Ursae Majoris (AR UMa) is presented, along with high-speed photometry. AM Her shows a variety of high states with frequent transitions between them. TESS photometry of AR UMa in the low state reveals no evidence of accretion, while the McDonald 2.1 m telescope caught AR UMa in its high accretion state. Roche-lobe overflow is shut off during low states of AR UMa, while accretion often still takes place during low states of AM Her. We derive inclinations of  $50^\circ$  and  $70^\circ$  for AM Her and AR UMa respectively. To model the high-state light curves of AM Her, we employ a self-organized map light-curve classification scheme to establish common accretion configurations. The cyclotron radiation properties then allow the production of emission region maps on the surface of the white dwarf. The accretion geometry of AM Her is most consistent with a multipolar field structure. The high-state photometry of AR UMa has stochastic accretion flaring, which we attribute to magnetically buffered mass transfer through the inner Lagrangian point L1. To consider this possibility, we examine the magnetism of both stars and argue that the local magnetic field near L1 can initiate short-lived accretion events and affect transitions between high and low accretion states in both AM Her and AR UMa. In particular, AR UMa has the low state as its default, while AM Her and most other active polars are in the high state by default.

*Unified Astronomy Thesaurus concepts:* [Magnetic stars \(995\)](#); [White dwarf stars \(1799\)](#); [Cataclysmic variable stars \(203\)](#); [Stellar accretion \(1578\)](#); [Accretion \(14\)](#)

## 1. Introduction

AM Herculis (AM Her) and AR Ursae Majoris (AR UMa) are nearby members of the class of the highest field (10–235 MG) magnetic cataclysmic variables (mCVs) known as polars due to the highly polarized optical radiation they emit. The cause of AM Her's occasional and dramatic variability in brightness and the connection to the underlying variability of the accretion rate, especially in contrast to AR UMa, is still not well understood. There are two aims for the current work: (1) to shed light on the character and mechanism for accretion rate variability in polars, generally known as low states and high states, and to address the question of why these fluctuations occur so frequently in AM Her, while AR UMa spends most of its time in the low state; and (2) to constrain the structure of the white dwarf (WD) magnetic field configuration, specifically to test complex, dipole plus quadrupole, models of the magnetic field for the WD.

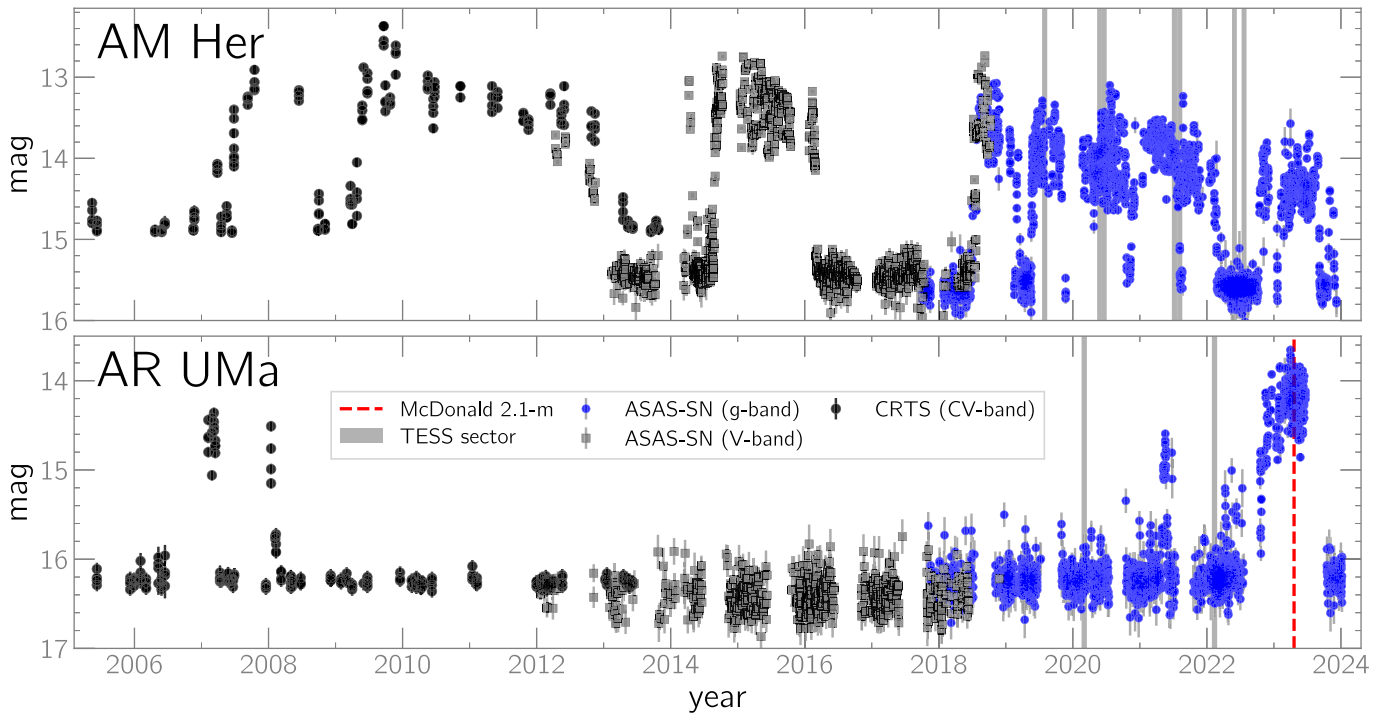
The low-state observations of AM Her and AR UMa are important in these aims because they allow constraints on the binary system parameters, especially the inclination, since other parameters are well constrained by a variety of multiwavelength data. High-state photometry allows for cyclotron modeling of the active accretion regions on the surface of the WD. While the current work is focused on the comparison of these two highly magnetic CVs, it is important to note that H-rich CVs with undetected magnetic fields, e.g., the UX UMa and VY Scl nova-like systems, as well as the He-rich AM CVn systems, also display dominant high states, occasional and unpredictable low states, and sometimes long-lived low states, with rare, short-duration high states. See Inight et al. (2022) for a recent paper on a UX UMa-type binary and Duffy et al. (2021) for a study of eight AM CVn systems. Magnetic effects from active regions and magnetic stellar winds from the donor star likely play a role in mass transfer in CVs containing either highly magnetic or some weakly magnetic WDs.

### 1.1. AM Her

AM Her is the brightest, one of the closest ( $d = 87.93 \pm 0.24$  pc; Bailer-Jones et al. 2021), and first identified polar.



Original content from this work may be used under the terms of the [Creative Commons Attribution 4.0 licence](#). Any further distribution of this work must maintain attribution to the author(s) and the title of the work, journal citation and DOI.



**Figure 1.** Multiyear light curves of AM Her and AR UMa obtained using the CRTS and ASAS-SN surveys. High and low accretion states, and sharp transitions, are observed in both cases. These two polars span the range in polar magnetic field strengths at 13 MG and 235 MG respectively. Both have shown consistent duty cycles over long baselines, with AM Her in the high state  $\sim 50\%$  of the time while AR UMa spends  $\sim 5\%$  in the high state. The times of TESS observations are indicated by shaded regions, and the McDonald 2.1 m photometry occurred at the very end of the AR UMa light curve.

Fifty years after being classified as a variable star by M. Wolf in 1924, AM Her was found to possess a peculiar spectrum with strong emission lines of H and He and a blue continuum (Bond & Tifft 1974). Soon after, the X-ray source 3U 1809+50 was found to vary with the same orbital period,  $P_{\text{orb}} = 3.09$  hr, as is seen in the optical photometry (Hearn & Richardson 1977), leading to the connection of the 3U X-ray source with AM Her.

In an unprecedented fashion, the study of accretion onto highly magnetized WDs began when Tapia et al. (1976) and Tapia and In (1976) detected up to  $\sim 10\%$  linear and circularly polarized optical radiation from AM Her. Many studies soon followed up this discovery (Cowley & Crampton 1977; Greenstein et al. 1977; Priedhorsky 1977; Szkody & Brownlee 1977; Tapia 1977), ultimately leading to a description of AM Her as a magnetic WD accreting from a low-mass M-type dwarf companion via an accretion stream directly (without an intervening disk) onto the magnetic poles of a  $\sim 10$  MG WD (Chanmugam & Wagner 1977, 1978; Stockman et al. 1977; Priedhorsky & Krzeminski 1978). The discovery of similar optically polarized X-ray sources—AN UMa, VV Pup, EF Eri, and others—led to the establishment of the subclass of CVs known as AM Herculis-type binaries or polars; see the review by Cropper (1990). For a review of X-ray light curves of AM Her and their analysis, see Schwobe et al. (2020), and for a review of accretion theory of polars and structures of magnetic field-channeled flow in CVs, see Wu (2000).

Several features of the AM Her light curve were found early on, but a complete understanding remains elusive. First, Hudec & Meinunger (1976) found, from archival plate studies, that AM Her undergoes transitions from bright states, with high accretion rates, to faint states, with low or even absent accretion. Long-term light-curve studies have shown AM Her to have a roughly 50/50 duty cycle for high/low states, as can

be seen in Figure 1, which shows the long-term (17 yr) light curves for AM Her and AR UMa from the Catalina Rapid Transit Survey (CRTS) and the All-Sky Automated Survey for Supernovae (ASAS-SN). AM Her shows a mixture of long and short, low and high, states, which can last from several days to months for low states, to several months to years in the case of high states. In stark contrast, AR UMa displays short-lived high states (Mason & Santana 2015; Duffy et al. 2022). One of the goals of this paper is to address this contrasting behavior.

EXOSAT observations of AM Her (Heise et al. 1985) indicated that the brightest soft X-ray emission in AM Her had unexpectedly moved from the secondary accretion region while the hard X-rays had remained present in the primary region. Heise et al. attributed this to a change in the relative accretion rates onto the two poles, called the reversed mode of accretion. Paradoxically, Mazeh et al. (1986) examined the optical light curves of AM Her during the reversed mode and found no change in the optical light curve, except for a slight overall decrease in brightness. X-ray observations from 2015 of the reversed mode found that its onset was not triggered by a significant change in the accretion rate (Schwobe et al. 2020). During low states of AM Her, little or no accretion takes place. During low-state observations using the International Ultraviolet Explorer, the low-state ultraviolet spectra do not show the emission lines that dominate the high-state ultraviolet spectra (Mason et al. 1992). Analysis of high–low state duty cycles and state transitions for AM Her has been performed (Kafka et al. 2005; Wu & Kiss 2008; Kalomeni 2012; Šimon 2016) with consistent results.

The WD magnetic field in AM Her, measured during low states using Zeeman spectroscopy, is 13 MG (e.g., Silber et al. 1996, see our Table 1) and appears to be complex. Wickramasinghe et al. (1991) found that during the high state

**Table 1**  
Binary and Stellar Parameters of AM Her and AR UMa

System Parameter	AM Her	AR UMa
Orbital period (hr)	3.094	1.932
$M_1 (M_\odot)$	$0.63_{-0.08}^{+0.10}$ (1)	$0.91-1.24$ (2)
$M_2 (M_\odot)$	0.20 (3)	0.154 (3)
$q = M_2/M_1$	$0.3175_{-0.0465}^{+0.0436}$	$0.124-0.169$
$T_1$ (K)	$19, 248_{-450}^{+486}$ (1)	$20,000 \pm 5000$ (4)
$T_2$ (K)	$3290 \pm 70$ (4), $3300$ (3)	$3200$ (2), $3177$ (3)
$R_1 (R_\odot)$	$0.013_{-0.0014}^{+0.0017}$ (1)	...
$R_2 (R_\odot)$	0.289 (3)	0.190 (3)
$B_1$ (MG)	13 (5), 14.5 (6)	230 (7), 235 (8)
Donor spectral type	M4.5V (9)	M5.5V (10)

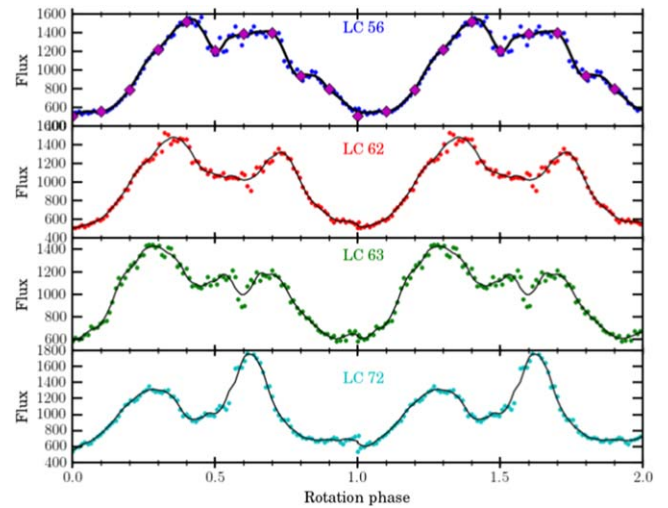
**References.** (1) Pala et al. (2022); (2) Bai et al. (2016); (3) Knigge et al. (2011; semiempirical relation); (4) Gänsicke et al. (2001); (5) Silber et al. (1996; Zeeman); (6) Bailey et al. (1991; cyclotron); (7) Schmidt et al. (1996); (8) Ferrario et al. (2003); (9) Young et al. (1981); (10) Harrison et al. (2005).

of AM Her, the material accreted onto two distinct regions on the WD: a primary column and a secondary one. The primary region is believed to occupy part of the WD face on the far side of the donor and accounts for the majority of the mass transfer and emission. The secondary accretion region is found on the surface of the WD facing the donor star, but at a separation substantially less than  $180^\circ$  from the primary region. This fact excludes the simplest model for explaining the behavior seen in AM Her, namely that of a centered dipole. Wickramasinghe & Wu (1991) presented a multipole model comprising a dipole and quadrupole in the WD and an intrinsic dipole in the donor star, and further elaborated it in Wu & Wickramasinghe (1993) to explain the observations of accretion geometry and distribution of magnetic field strengths between the accretion regions. While the model explained the general accretion in AM Her, and for most polars, the precise binary parameters and hence reliable locations of the accretion regions constitute the second goal of this paper, with the aim of constraining magnetic field structure.

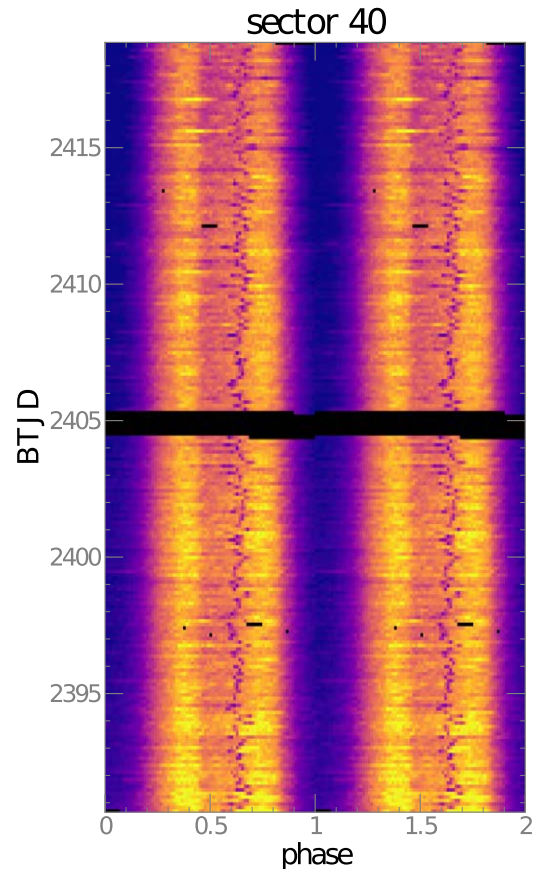
In order to characterize the various accretion states, the  $\sim 1000$  Transiting Exoplanet Survey Satellite (TESS) light curves of AM Her are studied in the next section. This variety is illustrated by the example light curves shown in Figure 2 and the two-dimensional (2D) light curve in Figure 3, which shows all of the light-curve data across a full sector.

### 1.2. AR UMa

AR UMa has the highest magnetic field ( $B = 235$  MG) among polars (Schmidt et al. 1996; Ferrario et al. 2003), and like AM Her it is one of the closest ( $d = 98.62 \pm 0.52$  pc; Bailer-Jones et al. 2021). The orbital period is  $P_{\text{orb}} = 1.932$  hr. Binary and stellar parameters for AM Her and AR UMa are given in Table 1. The light curve of AR UMa during the low state has a pronounced doubled-humped shape (Remillard et al. 1994; Szkody et al. 1999; Howell et al. 2001) and a single-peaked wave centered near phase 0.4 during high states (Szkody et al. 1999). In addition, the WD magnetic axis is closely aligned with the WD spin axis, but the dipole is twisted by about  $90^\circ$  in azimuth such that it lies nearly perpendicular to the stellar line of centers (Schmidt et al. 1999). The stronger pole does not accrete as much as the weaker one, as is typical for polars. From Hubble Space Telescope (HST) observations a WD temperature of



**Figure 2.** Selected, Sector 14, high-state light curves of AM Her. The labels such as LC 56 correspond to the sequential count of orbital light curves from Sector 14. The light curves during this high-state sector usually exhibit two maxima of varying intensity and phasing and a single minimum. In the light curve in the third panel from the top (green), and somewhat in that in the second panel (red), a narrow dip is seen near phase 0.6, which is attributed to an eclipse of an accretion region on the WD surface by the accretion stream.



**Figure 3.** The TESS Sector 40 data from AM Her are shown in 2D format and phased with the orbital period. A narrow feature is seen to wander in phase between 0.6 and 0.7, which is interpreted as a dip due to the accretion stream blocking a significant portion of the optical light from the accretion region of the WD. The minimum intensity occurs at zero phase (purple) and the maximum occurs near phase 0.4 (bright yellow). The data gap is shown in black across the center, as are some defects removed from the analysis. No sliding window function is used.

$20,000 \pm 5000$  K was derived by Gänsicke et al. (2001), who also estimated a magnetic field of  $B = 160$  MG for the weaker pole, consistent with  $B = 154$  MG from Ferrario et al. (2003). Doppler tomography indicates that the WD accretes via two funnels that split off from the ballistic gas stream, relatively close to the donor star (Schmidt et al. 1999).

### 1.3. Radio Emission

AM Her and AR UMa are well observed, persistently detected radio polars. Because we address the interaction between the WD and the donor magnetic field in the discussion section and the latter is detectable by radio emission, a brief review of the radio observations of mCVs is given here.

#### 1.3.1. AM Her

The first radio detection of an mCV was that of AM Her at 4.9 GHz using the Very Large Array (VLA; Chanmugam & Dulk 1982). A flux density of 0.67 mJy was measured to be relatively constant over the orbital cycle. The observations were made in full polarization mode and no circular polarization was observed. The authors concluded that this persistently detected radio emission from AM Her is due to gyrosynchrotron emission from energetic ( $\sim 350$  keV) electrons, and harmonic numbers 30–50 trapped in the WD magnetosphere. Additional VLA observations detected an essentially 100% circularly polarized flare with a flux of 9.7 mJy, which is about 20 times the quiescent emission.

Because AM Her’s persistently detected radio emission was just above the sensitivity limit of the original VLA, subsequent searches for radio emission from other mCVs using the VLA were largely unsuccessful (Bastian 1987; Beasley et al. 1994; Mason et al. 1996), except for the propeller Intermediate Polar (IP), AE Aqr (Bookbinder & Lamb 1987). However, several other studies were partially successful: Wright et al. (1988) used the Parkes 64 m telescope to detect the polar V834 Cen at 8.4 GHz; Pavelin et al. (1994) used the Jodrell Bank broadband interferometer to detect the two IPs AE Aqr and DQ Her, and the three polars AM Her, BG CMi, and ST LMi during observations of 21 mCVs. These studies combined resulted in the radio detection of only six mCVs with many upper limits and AM Her remained the only known persistently detected radio polar.

During a subsequent enhanced VLA survey, discussed further below, AM Her was detected three times: twice at 5.5 GHz with flux densities of  $102 \pm 9$  and  $104 \pm 8 \mu\text{Jy beam}^{-1}$  and once at 9.0 GHz with  $184 \pm 15 \mu\text{J beam}^{-1}$ . The circular polarization varied between 0% and 30% (Barrett et al. 2017, 2020, 2023, private communication). AM Her was also observed using the European VLBI Network at 5 GHz (Gawroński et al. 2018). From six astrometric measurements, they derived a distance of  $88.6 \pm 0.6$  pc, consistent with the Gaia result. It was observed mostly in the low accretion state, when the radio emission was at about 0.3 mJy, which is about a factor of two lower than that typically observed in the high state (e.g., Chanmugam & Dulk 1982; Mason & Gray 2007), suggesting that active accretion may enhance radio emission by increasing the supply of electrons. Gawroński et al. (2018) further suggest that (during this low state) the radio flux of AM Her was weakly modulated with the orbital motion, thus supporting the suggestion (Mason & Gray 2007) that magnetic reconnection takes place and radio-emitting electrons are accelerated near the L1 point, likely due to the interaction between the donor and the WD magnetic fields.

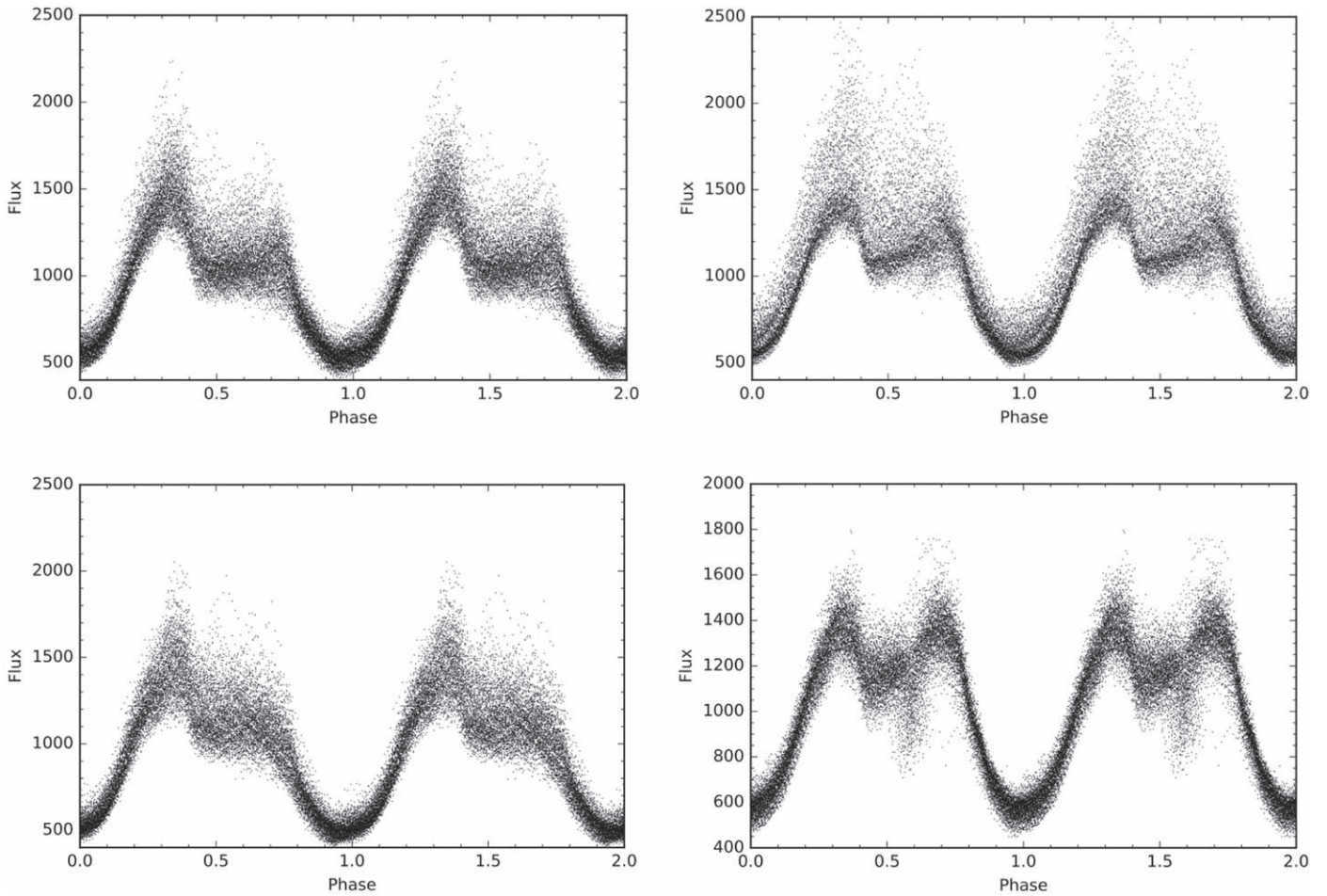
#### 1.3.2. AR UMa and the Enhanced VLA Survey

Interest in radio observations of mCVs was rekindled when Mason & Gray (2007) detected persistent radio emission from the polar AR UMa at a flux density of  $\sim 0.6$  mJy and flares up to  $1.122 \pm 0.195$  mJy at 8.4 GHz during a VLA survey of nine polars. Only AM Her and AR UMa were detected in that survey. However, after a major enhancement of the VLA increased its sensitivity by an order of magnitude, a large radio survey of mCVs was conducted by Barrett et al. (2017, 2020, 2023, private communication) at three frequencies (5.5, 9.0, and 21.0 GHz) to observe 195 mCVs, yielding 56 mCV detections. As a result, AR UMa was detected five times: twice at 5.5 GHz with flux densities of  $379 \pm 18$  and  $461 \pm 17 \mu\text{Jy beam}^{-1}$ , twice at 9.0 GHz with  $415 \pm 16$  and  $456 \pm 16 \mu\text{Jy beam}^{-1}$ , and once at 21.0 GHz with  $115 \pm 29 \mu\text{Jy beam}^{-1}$ . Only the K-band (21.0 GHz) detection showed high circular polarization of  $-77\% \pm 26\%$ . The other measurements were essentially unpolarized.

#### 1.4. Radio Emission and the Current Goals

The high brightness temperature ( $T_B \gtrsim 10^{10}$  K) requires coherent radio emission. Two possible emission mechanisms were suggested: plasma emission and electron cyclotron maser emission (ECME). Plasma emission occurs at the fundamental and second harmonic of the local plasma frequency. However, only the fundamental emission can be highly circularly polarized. The density required for the emission at 4.9 GHz is  $\sim 3 \times 10^{11} \text{ cm}^{-3}$ , which may exist very near the surface of the red dwarf donor. However, Dulk et al. (1983) argue that this emission is likely to be highly attenuated by the ambient plasma and therefore is unlikely to be the cause. ECME is the more likely mechanism, with the emission probably originating from the second harmonic in a magnetic field of  $\sim 1$  kG. If the plasma frequency is greater than the gyrofrequency, then the ECME cannot escape the plasma. This constrains the plasma density to be  $< 3 \times 10^{11} \text{ cm}^{-3}$ . The lower corona of the red dwarf is a likely emission region. Such an ECME needs a source of high-energy electrons, which may be provided by magnetic reconnection events due to the mutual interaction of the fields of the two stars.

Recall that the first goal of this paper is to investigate possible mechanisms driving accretion state transitions in polars. An important discovery from the observations of Barrett et al. and relevant to the present study is that  $>75\%$  of detected radio mCVs show highly ( $>50\%$ ) circularly polarized emission, which is characteristic of ECME or magnetized plasma emission and can be used to measure the magnetic field strength within the emitting plasma. Measurements of the high magnetic field of CV donors help motivate the current analysis of an interactive magnetic valve involved in the maintenance of and transitions between high and low mass-transfer states of polars. The large sample of radio-detected mCVs (Barrett et al. 2017, 2020) also shows that, if the radio emission is from the lower corona of the donor star, then its magnetic field strength, and hence magnetic dynamo, does not decrease appreciably when the donor star loses enough mass to become fully convective at an orbital period of about 3 hr. Magnetic braking must therefore still be a significant contributor to the loss of orbital angular momentum.



**Figure 4.** TESS photometry of AM Her during high accretion states, from Sectors 14, 25 (top), 26, and 40 (bottom), are shown folded with the orbital period. Note that Sector 40 (bottom right) is scaled differently than the other three and it shows the dip, also shown in the 2D light curve of Figure 3 and attributed to the phase-dependent blocking of the accretion spot by the stream.

## 2. Observations

For each sector, TESS (Ricker et al. 2015) collects photometric data for about 28 days continuously, except for a gap of about 2–3 days in the middle, near perigee, so each sector consists of two parts with roughly 13 days of continuous data. The data were extracted from the TESS database (Team 2021) using the lightkurve software. The TESS bandpass is similar to a combined  $R$  and  $I$  filter, thus, it is dominated by cyclotron radiation emitted by polars in the high accretion state. All of the photometry presented here was obtained at 120 s cadence.

### 2.1. AM Her

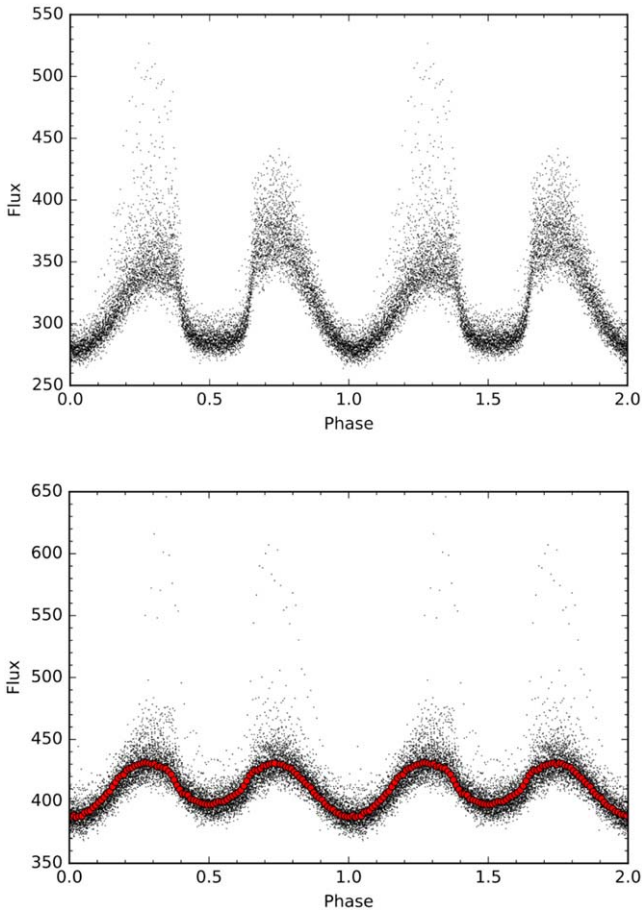
Starting in 2019 July, AM Her has been frequently observed by TESS. This paper addresses the first seven sectors of data on AM Her: Sector 14 (2019 July 18 to 2019 August 15), Sector 25 (2020 May 13 to 2020 June 8), Sector 26 (2020 June 8 to 2020 July 4), Sector 40 (2021 June 24 to 2021 July 23), Sector 41 (2021 July 23 to 2021 August 20), Sector 52 (2022 May 18 to 2022 June 13), and Sector 54 (2022 July 9 to 2022 August 5). See Figure 1, which shows the TESS epochs on the long-term light curves. Selected light curves from AM Her show variations in their morphology that are due to changes in the cyclotron emission regions (see Figure 2 and the 2D version in Figure 3). In Figure 4, the high-state TESS data are shown folded on the orbital period. There are significant sector-to-

sector variations as well as variations within each sector. In Figure 5 the low-state photometry of AM Her is displayed. Examples of short-term flares during low states are shown in Figure 6. Similar short,  $\sim 1$  day, accretion or active donor flare events in AM Her have been reported previously (Mason et al. 1994).

In order to characterize variations in both high- and low-state TESS orbital light curves, three measurements were obtained and are plotted in Figure 7. The measurements are the photometric minima (red squares), the photometric maxima or peak intensities (blue dots), and the phase of the accretion stream dip (magenta crosses), the last seen only in Sector 40 photometry (see also the bottom right panel of Figure 4). The peak intensities are shown to vary from one cycle to the next, often being accompanied by a secondary, and rarely a third, peak. In contrast, the minimum intensities are shown to be relatively stable.

#### 2.1.1. AM Her: Spin/Orbital Ephemeris

We performed a period search analysis in three ways. First, all of the high-state minima were measured and least-squares analysis was performed. Then, a phase dispersion minimization (PDM) period search was performed for the high- and low-state data separately. These were found to be consistent, with the most reliable deemed to be the PDM of the low-state data



**Figure 5.** Low state photometry of AM Her obtained during Sector 41 (second half) and Sector 52 is shown folded on the binary period. Brief,  $\sim 1$  day, accretion events were observed. The nonflaring part of the light curve, from Sector 52, is binned into 100 bins for binary light-curve modeling.

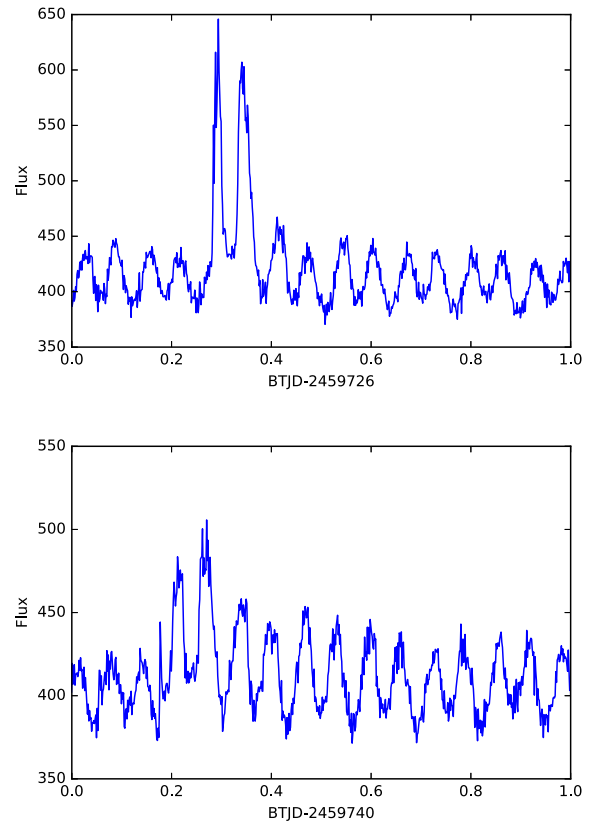
(Sectors 41:part 2 and 52), yielding a photometric period of  $P = 0.1289271(1)$  days, which is also consistent with the orbital ephemeris (Schwarz et al. 2002; Kafka et al. 2005) that defines the inferior conjunction of the donor star and is derived from the blue-to-red crossing of the narrow emission-line component. We phased all of the TESS data using the Schwarz et al. (2002) ephemeris as it still appears not to require an update (also see Schwöpe et al. 2020), especially based on its accurate phasing of minima in Sector 52, low state (Figure 5). Hence, the (spectroscopic) orbital ephemeris,

$$T_0(\text{BJD}) = 2451763.453266 + 0.128927103(6)E,$$

is used to obtain the phased and folded TESS photometry during high states, which are shown in Figure 4, and during low states, in Figure 5.

### 2.1.2. Accretion Stream Dips

In some polars, especially in eclipsing systems, there is a significant drop in brightness lasting  $\sim 5$  minutes and attributed to an eclipse of the accretion region on the WD by the accretion stream, e.g., CRTS J0350+3232 (Mason et al. 2019), see also Watson (1995). During only one sector of TESS observations, AM Her displays what appears to be a stream eclipse dip. In Figure 3, a 2D version of the TESS light curve from Sector 40 is shown. Sector 40 is phased with the orbital period and formatted in a two-dimensional (2D) structure with time

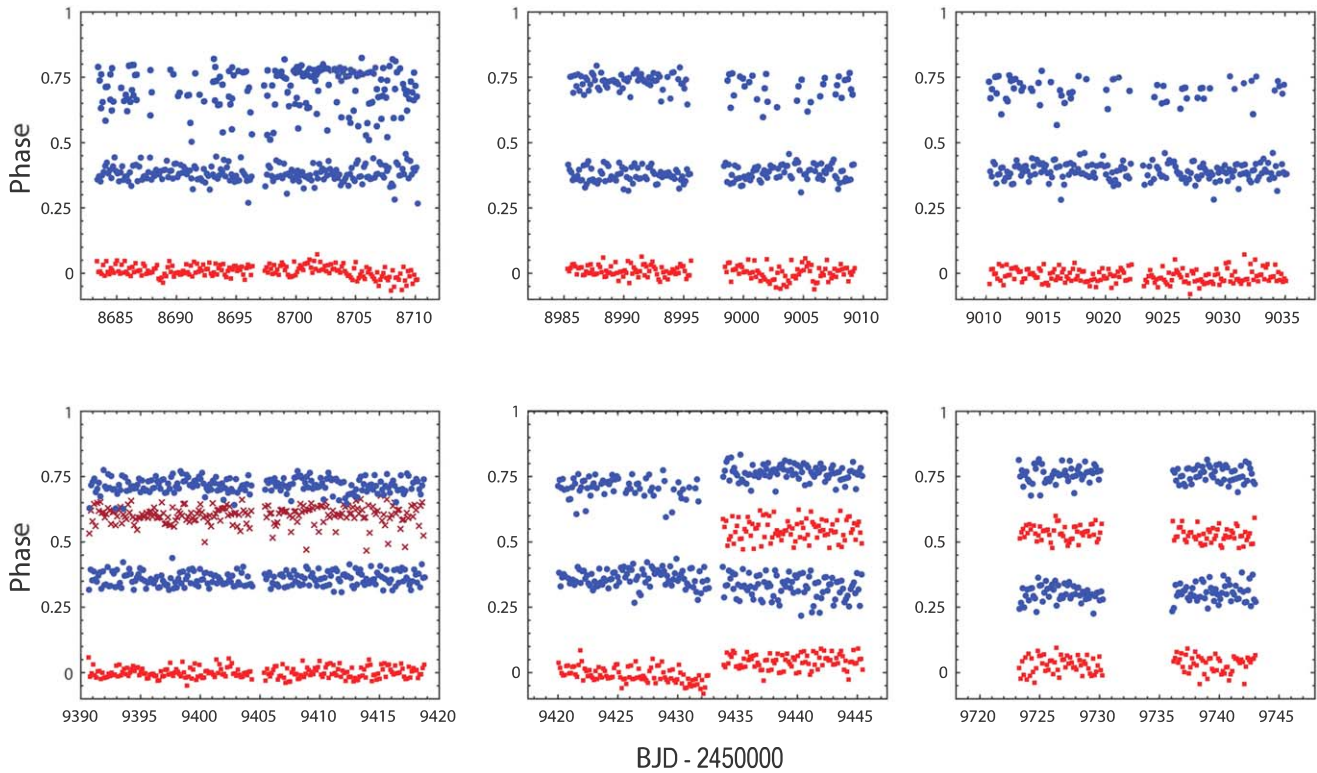


**Figure 6.** Short-lived high states during the prolonged low state of Sector 52. Enhanced accretion occurred for a single orbital cycle, and these two events are 14 days apart.

beginning at the bottom of the figure. At zero orbital phase, the purple intensity level, the minimum intensity occurs. The maximum intensity, shown in yellow, occurs at about phase 0.4. The gap, a black strip across the center, is a data gap. Some defects appear and have been removed for analysis. Bright spots indicate short-lived increases in the accretion rate. The stream dip shifts erratically between phase 0.6 and 0.7 on the timescale of a few orbital cycles. Measurements of the stream eclipse dip were made—see Figure 8—which show a relationship between the depth of the dip and its orbital phase.

### 2.1.3. AM Her: Binary Parameters

TESS photometry obtained during the low state of polars provides an opportunity to perform high-quality fits using the Wilson–Devinney binary modeling software. This is because in low states, with the near or complete absence of accretion, the emission sources are relatively simple and well understood. The luminosity of the WD is given by its effective temperature  $T_1$  and its radius  $R_1$ . The radius in turn is related to the WD mass,  $M_1$ , through an observed and theoretically understood mass–radius relation, which is dependent somewhat on composition. The donor star in polars is close to precisely filling its Roche lobe, so it has a precisely defined nonspherical shape, given the binary period  $P$  and the masses  $M_1$  and  $M_2$ , which when projected into the line of sight produces a light curve that depends strongly on the inclination of the binary.  $T_1$  feeds back into the analysis because the WD is much hotter than the donor, so it heats the donor on the side facing the WD. Hence, low-state polar light curves are well described by ellipsoidal variations of the donor along with a component due



**Figure 7.** Measurements of light-curve features are shown from Sectors 14, 25, and 26 (top) and Sectors 40, 41, and 52 (bottom). Light-curve maxima are shown as blue dots (both primary and secondary maxima), minima are red squares (secondary minima are seen only during the low state, in Sectors 41 and 52), and the accretion stream dip as magenta crosses (seen only in Sector 40). Measurements in Sector 54 are similar to those in Sector 52 and are not shown.

to the reflection effect of the donor intercepting and re-emitting radiation from the much hotter WD. The WD is modeled as a spherical single-temperature star, which we additionally constrain to follow the standard WD mass–radius relation. The donor star is constrained to be filling its Roche lobe with a mass set to be that presented in the semiempirical relation of Knigge et al. (2011), from which we also obtain  $T_2$  and  $R_2$ .

Fortunately, for AM Her the mass of the WD has been well constrained by UV spectroscopy to be  $0.63_{-0.08}^{+0.1} M_{\odot}$  and the WD radius is found to be  $0.013_{-0.0014}^{+0.0017} R_{\odot}$  (Pala et al. 2022). The WD temperature from UV observations during the low state of  $T_1 = 20,000$  K (Gänsicke et al. 1995, 2006; Silber et al. 1996) is consistent with the recent result of  $19,248_{-450}^{+486}$  K (Pala et al. 2022). On the other hand, there is some tension concerning the binary inclination of AM Her. There is no evidence for eclipses of the L1 point or the gas stream, which would occur around phase zero for high inclinations. Therefore, an upper limit of  $i < 76^{\circ}$  is inferred. Using linear and circular polarization measurements, an inclination of  $i = 35^{\circ}$  was obtained (Brainerd & Lamb 1985). A two-spot emission model was used to derive an inclination of  $i = 52^{\circ}$  (Wickramasinghe et al. 1991). From analysis of radial velocity data of AM Her, Davey & Smith (1996) derived a binary inclination of between  $45^{\circ}$  and  $60^{\circ}$ . High-precision photometry during the lowest of states reveals ellipsoidal variability, and modeling allows for a reliable, independent, and—if the stellar masses are known—precise determination of the inclination.

A Markov Chain Monte Carlo (MCMC) procedure was used to determine the best-fit Wilson–Devinney binary model parameters and uncertainties given the constraints described. The results for both binaries are given in Table 2. For AM Her it is reasonable to fix the well-constrained stellar masses  $M_1$

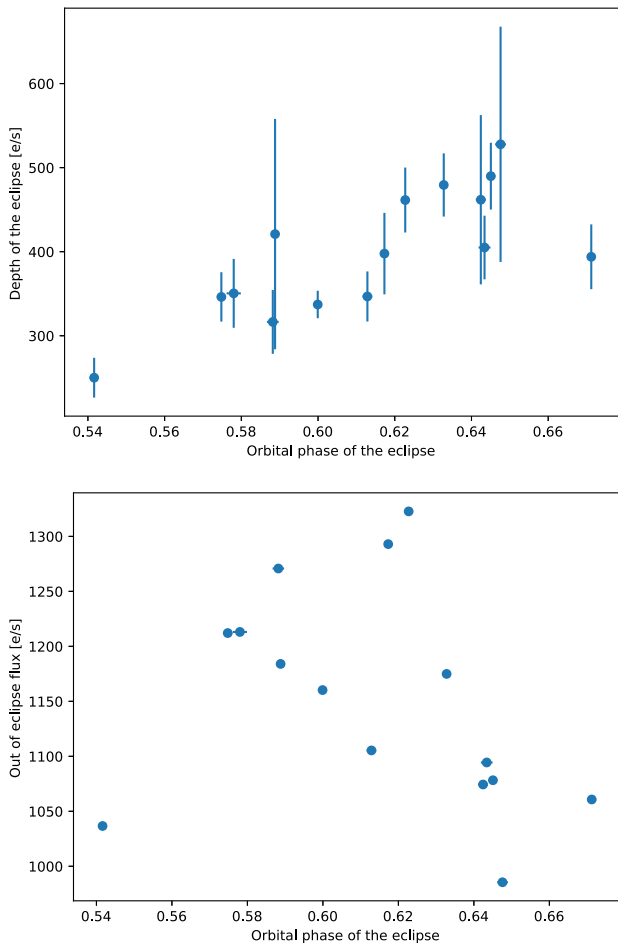
and  $M_2$ , and the Roche-lobe filling donor radius  $R_2$ , to set values and to let the inclination  $i$  and the WD temperature  $T_1$  vary. The result, shown in Figure 9, is slightly warmer than, although reasonably consistent with, the measurements of  $T_1$  given that the TESS bandpass is too red to have much sensitivity to  $T_1$ . The inclination of  $i = 50^{\circ}2 \pm 2^{\circ}0$  derived here using analysis of the low-state variability is a significant improvement in reconciling other independent derivations of  $i$ .

## 2.2. AR UMa

TESS observed AR UMa during Sector 22 (2020 February 18 to 2020 March 18) and Sector 48 (2022 January 28 to 2022 February 26). For both of these observations, AR UMa was in a low state with no signs of accretion at any time during either sector. The folded light curve for Sector 48 is shown in Figure 11. The data are coadded to produce an effective exposure time of 10 minutes. The figure includes the light curve averaged into 100 bins (red dots) for binary modeling.

### 2.2.1. AR UMa: A New Spin/Orbital Ephemeris

A new ephemeris for AR UMa is derived as follows. All of the unbinned data of AR UMa obtained during Sectors 22 and 48 are combined for a period search, yielding  $P = 0.08050062$  (4) days. This period is consistent with the ephemeris of Schmidt et al. (1999) within quoted uncertainties and that of Bai et al. (2016). The TESS data sets, which are separated by almost two years, are then simultaneously fitted with a best-fit sinusoidal function, with half the orbital period to match the ellipsoidal variations, phased with the Schmidt et al. (1999) zero-point, after conversion from HJD to barycentric JD (BJD). The new orbital period and original zero-point are mutually



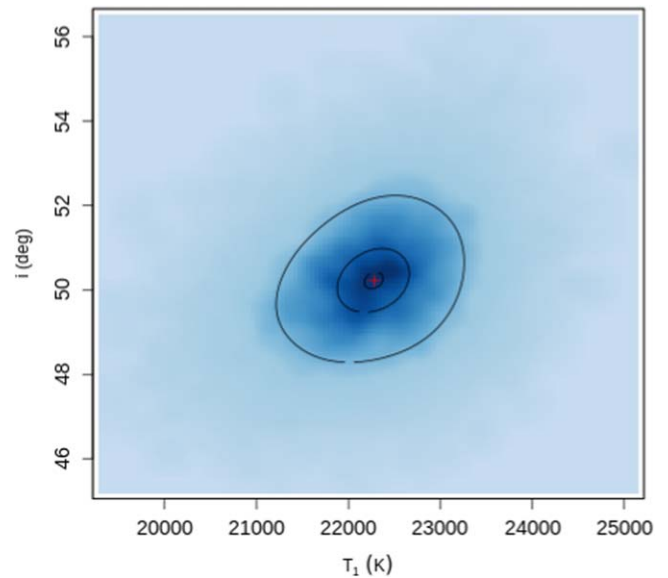
**Figure 8.** Measurements of the eclipse by the accretion stream of a cyclotron emission region from Sector 40. The top panel shows some correlation between the phase of the stream dip and the out-of-eclipse flux; the latter may be a proxy for the accretion rate. The bottom panel shows a significant relationship between the depth of the stream eclipse and the orbital phase of the eclipse.

**Table 2**

Binary Parameters Used for or Derived Using the Wilson–Devinney Binary Modeling (Wilson & Devinney 1971) of the Low States of AM Her and AR UMa

Model Parameter	AM Her	AR UMa
Orbital period (hr)	3.094	1.932
$M_1 (M_\odot)$	0.63 fixed (1)	$1.125 (3) \pm 0.075$
$M_2 (M_\odot)$	0.289 fixed (2)	$0.198 (3) \pm 0.001$
$M_2/M_1 = q$	0.3175 fixed	$0.1583 \pm 0.075$
$T_1$ (K)	$19,248^{+486}_{-450}$ (1)	$20,000 \pm 5000$ (4)
	$22,250 \pm 2500$ (11)	$22,250 \pm 2000$ (11)
$T_2$ (K)	$3290 \pm 70$ (4)	$3200$ (2), $3177$ fixed (3)
$R_1 (R_\odot)$	$0.013^{+0.0017}_{-0.0014}$ (1)	...
	0.0115(11)	0.00724 (11)
$R_2 (R_\odot)$	0.20 (3)	0.154 (3)
$B_1$ (MG)	13 (5), 14.5 (6)	230 (7), 235 (8)
Donor spectral type	M4.5V (9)	M5.5V (10)
Binary inclination $i$	$50^\circ 2 \pm 2^\circ 0$ (11)	$70^\circ 5 \pm 6^\circ$ (11)

**References.** (1) Pala et al. (2022); (2) Bai et al. (2016); (3) Knigge et al. (2011; semiempirical relation); (4) Gänsicke et al. (2001); (5) Silber et al. (1996; Zeeman); (6) Bailey et al. (1991; cyclotron); (7) Schmidt et al. (1996); (8) Ferrario et al. (2003); (9) Young et al. (1981); (10) Harrison et al. (2005); (11) this work.



**Figure 9.** An MCMC Wilson–Devinney binary model optimization of the low-state phased binned light curve of AM Her from Sector 52 (Figure 5 bottom). For this fit, only the WD temperature  $T_1$  and the inclination  $i$  are free parameters. The assumed and best-fit parameters are listed in Table 2. The red symbol indicates the maximum of the 2D distribution. The contours represent  $1\sigma$ ,  $2\sigma$ , and  $3\sigma$  confidence levels. Table 2 lists the  $3\sigma$  results.

modified to minimize  $\chi^2$  from the sinusoidal fit and to determine uncertainties. This allows for a slight refinement of the orbital period and a test for a period change. The best-fit ephemeris did not require a change to the zero-point, defined as the inferior conjunction of the donor star and coincident with the photometric minimum, except for the conversion to BJD. The new orbital ephemeris for AR UMa is given by

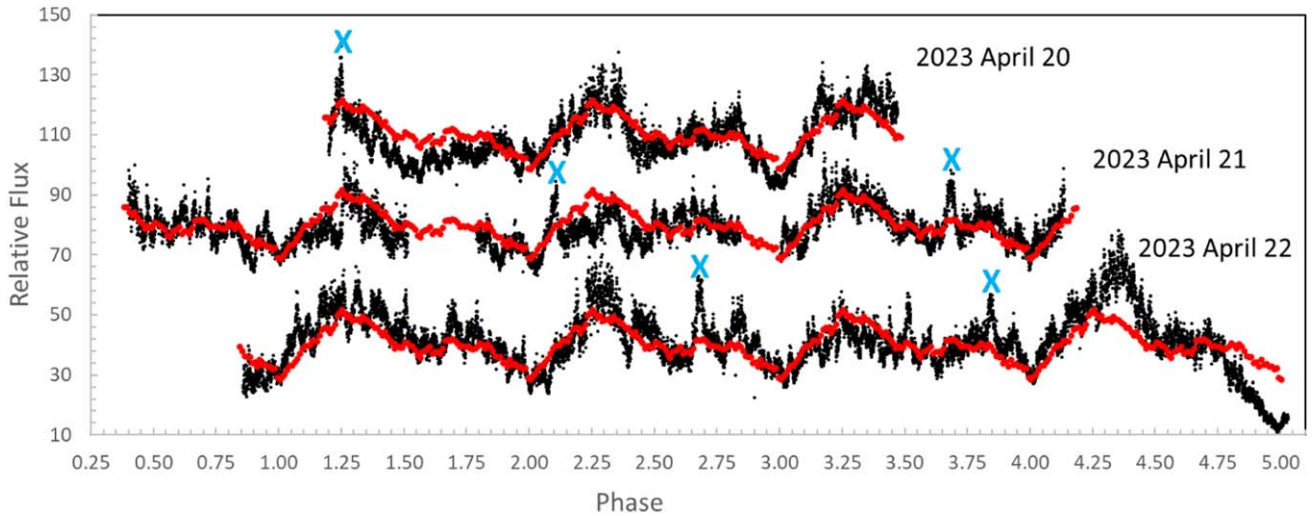
$$T_0(\text{BJD}) = 2450470.43166(6) + 0.0805006437(12)E.$$

Photometry of AR UMa was obtained using the McDonald Observatory 2.1 m telescope at 5 s time resolution on three nights: 2023 April 20, 21, and 22 (Figure 10). These data were obtained during the rare high state of AR UMa; recall Figure 1. Figure 10 shows dramatic variability characterized by flarelike bursts of accretion. These are most easily interpreted as magnetically controlled mass transfer at L1 although active donor flares are also possible. A possible mechanism for this behavior is presented in the discussion section.

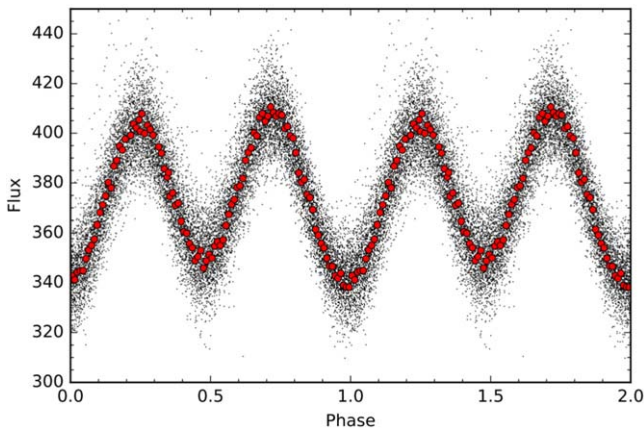
### 2.2.2. AR UMa: Binary Parameters

Originally, Schmidt et al. (1999) derived an accretion geometry from polarization and radial velocity measurements and obtained an inclination between  $40^\circ$  and  $60^\circ$  for AR UMa. Derivations using low-state photometric data have yielded higher inclinations. Near-IR modeling of low-state data was performed by Howell et al. (2001) using  $T_1 = 15,000$  K,  $T_2 = 3150$ ,  $q = 0.3$ , and  $M_1 = 0.6 M_\odot$  and they derived  $i = 70^\circ$ . However, the effective temperature of the WD in AR UMa is weakly constrained by HST observations to be somewhat higher,  $T_1 = 20,000 \pm 5000$  K (Gänsicke et al. 2001). This temperature is higher than expected given that AR UMa lies just below the lower boundary of the CV period gap with mass transfer driven by gravitational radiation. It should have a long-term low accretion rate, which means that we expect  $T_1$  to be 10,000–15,000 K; see Araujo-Betancor





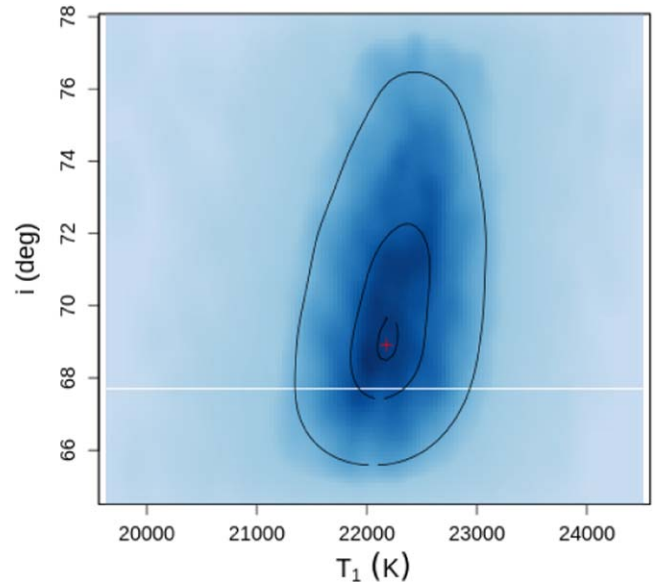
**Figure 10.** Photometry of AR UMa obtained using the McDonald Observatory 2.1 m telescope at 5 s time resolution on three nights, 2023 April 20, 21, and 22, phased on the new orbital ephemeris. Data on different nights are shifted vertically by 30 units for clarity. The red line is the median light curve derived from all of the data binned into 100 phase bins, shown repeated for comparison. Each night shows dramatic variability from the median due to flaring. Five flares are marked with a blue X. Weaker shorter-timescale flaring is also observed. This flaring and possibly also the large rise and drop at the end are short-lived accretion states that are attributed to magnetically controlled mass transfer from L1.



**Figure 11.** The TESS photometry of AR UMa during Sector 48 phase-folded with the orbital period. Both Sectors 22 (not shown) and 48 show the system in a low mass-transfer state. The strong variability is likely mainly due to binary ellipsoidal variations. The light curve is binned into 100 bins for binary light-curve modeling.

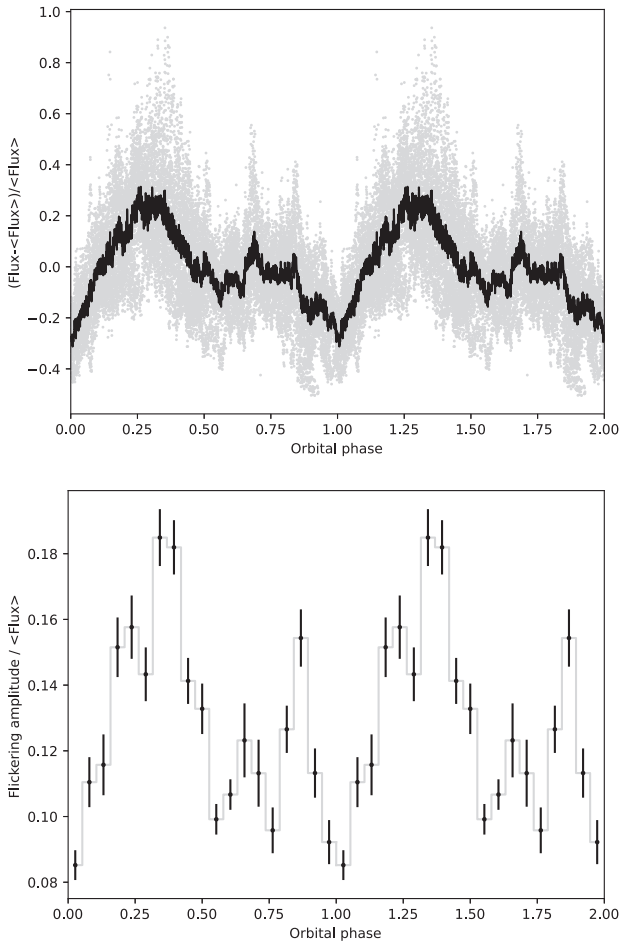
et al. (2005). Bai et al. (2016) used spectral decomposition to estimate the stellar parameters of the M dwarf donor and then used both the radial velocity curves of the  $H\beta$  emission line and the Na I absorption line to dynamically determine a rather high mass for the WD in AR UMa of between  $0.91$  and  $1.24 M_{\odot}$ .

The lack of eclipses also limits the available parameter space. With these constraints, the TESS data set allows for high-quality fits to the photometric data in Figure 11. The results of the Wilson–Devinney binary model optimization are listed in Table 2. Following a similar procedure to that described previously for AM Her, we employed standard theoretical considerations; however, the observations are not as well constrained for AR UMa as for AM Her. The key difference is that the precisely measured WD mass  $M_1$  for AM Her strongly constrains the solution because it determines the semimajor axis  $a$  and the Roche-lobe geometry, leading to strong constraints on the secondary. In addition,  $M_1$  constrains  $R_1$  through the WD mass–radius relation. For AM Her, we have



**Figure 12.** The result of a Wilson & Devinney (1971) binary model with MCMC optimization using the low-state phased binned light curve of AR UMa from Sector 48 (Figure 11). The red cross indicates the maximum of the 2D distribution. The contours represent  $1\sigma$ ,  $2\sigma$ , and  $3\sigma$  confidence levels. Table 2 lists the  $3\sigma$  results.

the luxury of a well-constrained WD, and consequently the light curve provides the final constraint, solving the system of equations and yielding the inclination. One caveat is that the difference in stellar temperatures ( $T_1 - T_2$ ) enters the light-curve analysis, and  $T_1$ , while constrained in the UV, is not well constrained in the TESS bandpass, which potentially introduces a systematic error. Now, because the WD mass  $M_1$  in AR UMa is less constrained, the solution involves three loosely constrained variables:  $M_1$ ,  $T_1$ , and  $i$ , rather than just two for AM Her:  $T_1$  and  $i$ . For this reason, many trial fittings were performed for AR UMa, and they strongly favored  $M_1$  in the middle of the proposed range; see Table 2. The MCMC analysis of the AR UMa light curve also provides a relatively strong constraint on the inclination—see Figure 12, but notice

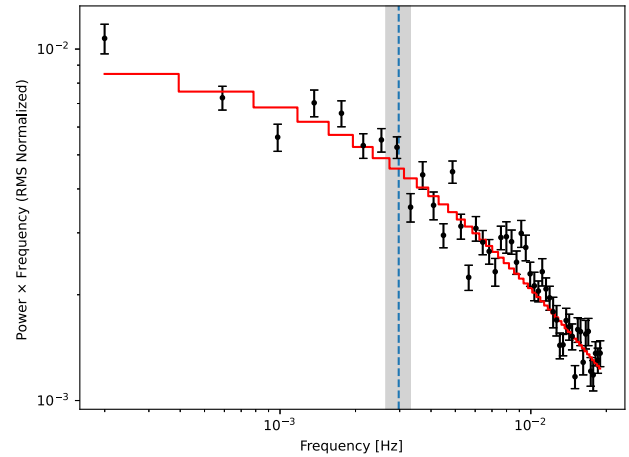


**Figure 13.** Top: the McDonald Observatory 2.1 m (3 s) normalized photometry phased with the orbital ephemeris as gray. The phased-average light curve is shown in black. Bottom: the light curve is further binned into 20 phase bins for variability analysis. The flaring amplitude is shown as a function of the orbital phase, with two cycles shown as usual for clarity.

that the  $3\sigma$  error circle is five times larger for AR UMa than for AM Her as shown in Figure 9, due mostly to the weaker constraint on the mass.

### 2.2.3. Flickering in the High State of AR UMa

Examination of the high-state, McDonald (3 s) photometry shown in Figure 10, covering  $\sim 9$  orbital cycles, quickly reveals two types of variability: (1) at least five flares that are likely short-lived accretion events (like those discussed in Duffy et al. 2022) and occur randomly with phase, and (2) a high degree of high-frequency variability, especially at particular phases, such as at phase 0.3 when AR UMa is at its brightest. We performed a flickering analysis in a manner similar to that done by Ilkiewicz et al. (2022). First, the data are phased with the orbital period and then a mean orbital light curve is calculated as shown in Figure 13, top panel. The resultant phase plot of flickering amplitude is of limited value since there are relatively few orbital cycles. We then binned the flickering amplitude into 20 equally spaced bins and calculated the rms error of flickering amplitude within each bin. Flickering from one pole is clearly visible between phases 0.0 and 0.5, with a strong peak at phase 0.3; see Figure 13, bottom panel. However, what happens at orbital phase  $> 0.5$  is quite puzzling. We are



**Figure 14.** The fit to the flickering analysis. The black points are measurements, the red line is the fit, the dashed blue line corresponds to the fitted break frequency, and the gray area corresponds to the break frequency error.

probably seeing flickering from the other pole, which is eclipsed right where the maximum should be. However, given the large number of flares observed during just a few orbital cycles, we do not want to overinterpret these results.

We also calculated the power density spectrum (PDS) of the AR UMa high-state light curve after the orbital variability was removed. The power spectral density was rms-normalized (Miyamoto et al. 1991; Belloni et al. 2002). Then a broken power law in a form from Equation (3) of Scaringi et al. (2012) was fitted and found to give a good fit; see Figure 14. As a result, we obtain a break frequency of  $0.0030 \pm 0.0004$  Hz. The corresponding value  $\log(f/\text{Hz}) = -2.52$  is what is expected for CVs; see Figure 11 of Dobrotka et al. (2020). If confirmed, AR UMa is the first polar with a measured break frequency in the PDS. We recommend more observations to confirm this result and to investigate its implications.

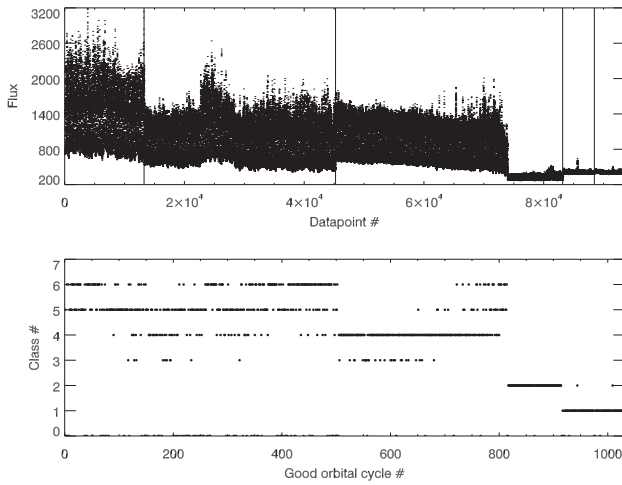
## 3. Cyclotron Modeling

The optical light curve of AM Her is highly erratic. Cycle-to-cycle variations can be attributed to shifts in the accretion configurations. As a result, averaging over light curves will erase the signatures of the different accretion states and mask transitions between them. Thus, in order to accurately characterize the typical states and track transitions between them, a light-curve classification process is used.

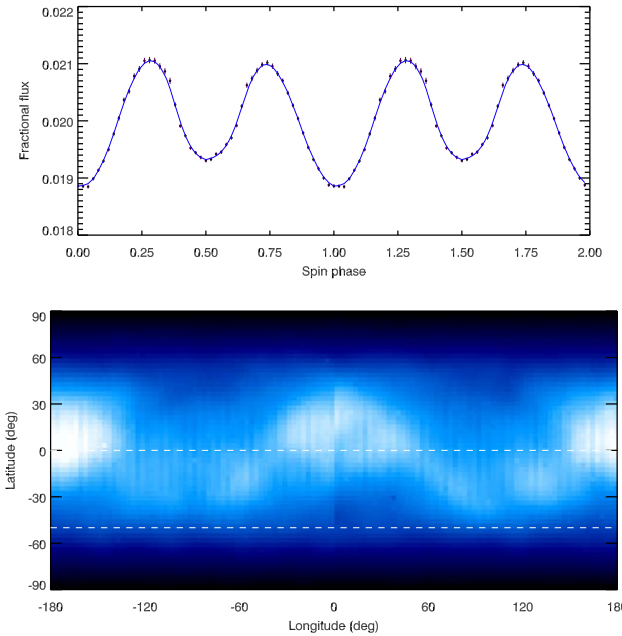
### 3.1. AM Her: Classifying Accretion States

Our procedure is based on self-organizing map (SOM) unsupervised learning (Kohonen 1990; see also Mähönen & Hakala 1995, and citations therein, for astronomical applications of SOM). Once model SOM light curves are generated for a set of typical states that we will call classes, cyclotron emission maps are calculated for each class.

To classify the accretion states in AM Her using SOM, we first created a uniform training set, by folding the data from each orbital cycle and then binning the folded data into 50 phase bins. The incomplete cases were removed. Additionally, pairwise correlations of these were examined in an attempt to see whether there is a typical separation in cycle count where the correlation would be better/worse than on the average, but

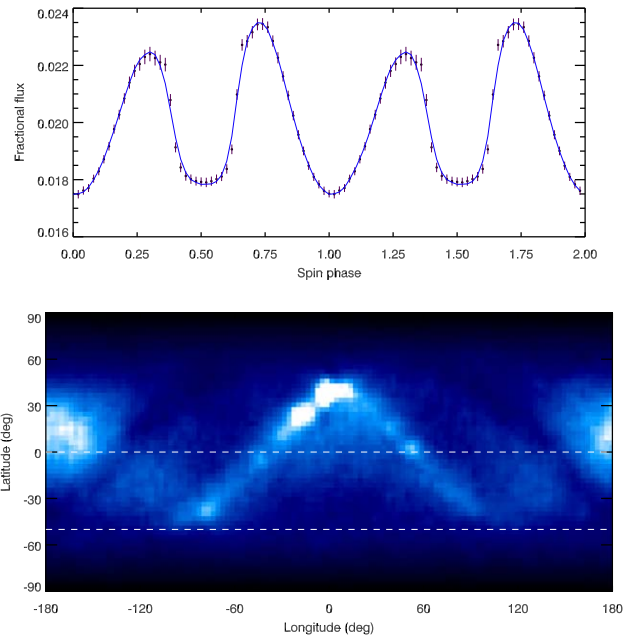


**Figure 15.** Top: TESS photometry of AM Her with the gaps removed. Bottom: the corresponding results of the SOM light-curve classification are shown so that comparisons between the light-curve class and its flux and variability may be made.



**Figure 16.** Cyclotron fits to determine class 1 spot positions assuming a binary inclination of  $50^\circ$ . Top: the class 1 light curve. Bottom: the bright blue and uniform background indicates that the resulting map does not show significant cyclotron emission, consistent with the observed modulation being due to ellipsoidal variations.

no such typical separation was found. Next, SOMs were created in an effort to classify the light curves into clusters or classes based on their pulse shape. Eventually, after some experimenting, six classes were deemed to describe the problem adequately. The SOM classification was performed on the full set of light curves (1032 orbital light curves) and each light curve was phased into 50 phase bins before classification. Of these, 920 were selected that had data covering the 50 phase bins without gaps. Figure 15 shows all the data points in chronological order (top panel), with vertical lines separating the data sets with large gaps between them. The bottom panel of Figure 15 shows the corresponding SOM classification of the light curves covering the same range. By



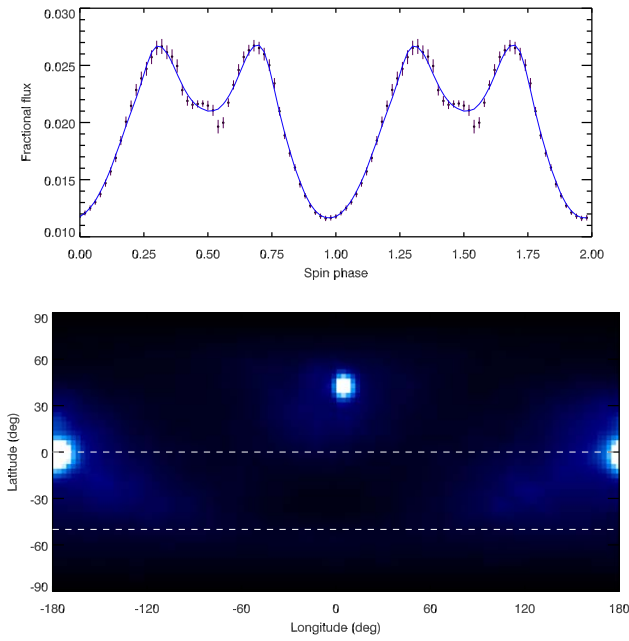
**Figure 17.** Cyclotron fits to determine class 2 spot positions assuming a binary inclination of  $50^\circ$ . Top: the class 2 light curve. Bottom: the resulting cyclotron map shows an emission spot or arc in the northern hemisphere superimposed on the ellipsoidal variations.

comparing the top and bottom plots, one may easily track how the flux level and variability in each sector relate to the results of the classification. This classification seems to establish a small set of accretion states and allows for cyclotron emission modeling of those accretion configurations.

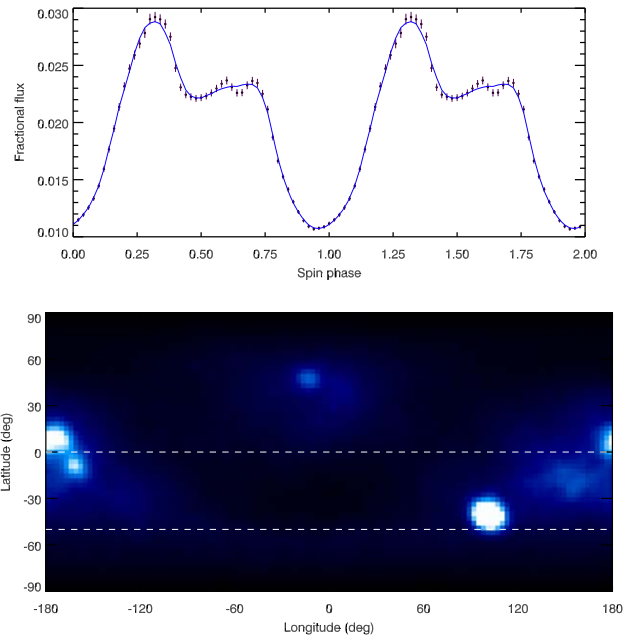
### 3.2. Cyclotron Emission Modeling

With the aim of constraining the WD magnetic field structure and accretion geometry, cyclotron emission maps of the surface of the WD in AM Her are made. The wavelength of the cyclotron emission depends on the magnetic field strength. The light curve is the result of one or more accretion columns on the WD surface. The radiation is beamed primarily at a right angle to the field originating just above the WD surface at the magnetic poles. This inversion, to map the cyclotron emission on the WD surface and thus to find spot locations, hinges on using a model of the angle dependence of the cyclotron emission. Specifically, the model grids in Wickramasinghe & Meggitt (1985) with plasma thermal temperature of 10 keV, emission region optical depth parameter  $\Lambda = 10^5 - 10^7$ , and cyclotron harmonics  $N_{\text{harm}} = 8$ , were used to match the known magnetic properties of the system (see Hakala et al. 2019 for the details of the method). A similar approach was also used in Cropper & Horne (1994), which assumed the emission is isotropic. However, here we relax the assumption of isotropic emission and consider a local cyclotron emission model. Also, we use a global differential evolution (DE)-based optimizer for the inversion. The regularization is carried out applying a maximum entropy principle, as in Cropper & Horne (1994). Note that in the absence of polarized flux data, used by Potter et al. (1998), the separation of cyclotron emission from opposite magnetic poles is potentially ambiguous.

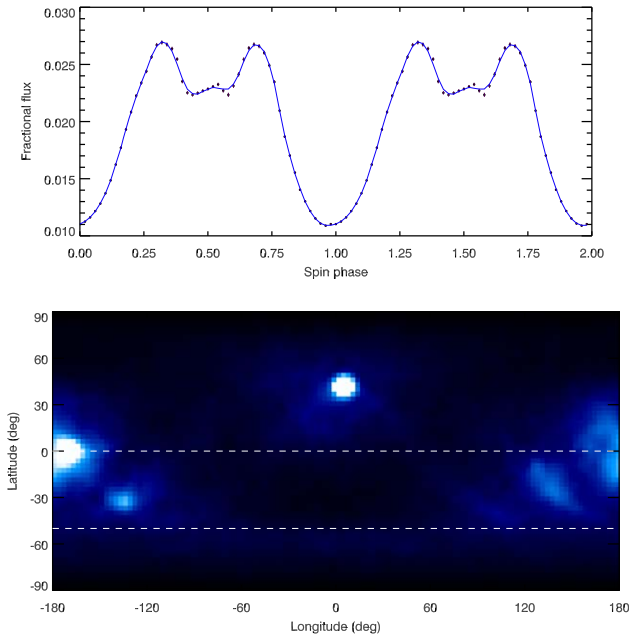
Separate cyclotron maps were computed for each of the six mean light curves derived from the SOM classification. The mean light curves with the resulting fits are shown in Figures 16, 17, 18, 19, 20, and 21 (top) with the resulting



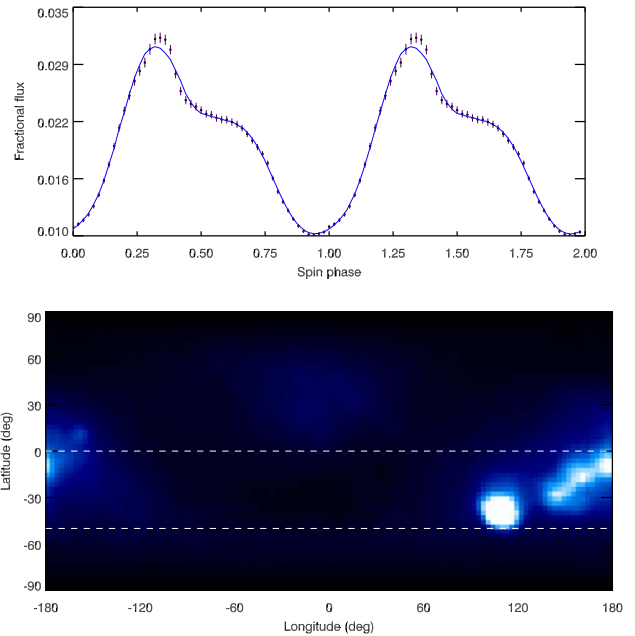
**Figure 18.** Cyclotron fits to determine class 3 spot positions assuming a binary inclination of  $50^\circ$ . Top: the class 3 light curve. Bottom: the resulting high-state cyclotron map displays two distinctive and well-located accretion regions, one of which is located on the equator on the opposite side to the WD.



**Figure 20.** Cyclotron fits to determine class 5 spot positions assuming a binary inclination of  $50^\circ$ . Top: the class 5 light curve. Bottom: the resulting high-state cyclotron map now shows a bright southern spot, a fainter equatorial spot, and just a hint of the northern spot.



**Figure 19.** Cyclotron fits to determine class 4 spot positions assuming a binary inclination of  $50^\circ$ . Top: the class 4 light curve. Bottom: the resulting high-state cyclotron map is similar to the class 3 case but more complicated.



**Figure 21.** Cyclotron fits to determine class 6 spot positions assuming a binary inclination of  $50^\circ$ . Top: the class 6 light curve. Bottom: the resulting high-state cyclotron map shows a bright southern spot accompanied by an equatorial arc.

cyclotron emission maps (bottom). The cyclotron maps are shown in a long.-lat. grid with  $X$  and  $Y$  axes referring to map pixels. The pixel size is  $3^\circ \times 3^\circ$ . The “north” pole is closer to Earth than the “south” pole.

We ran one of these sets a number of times in order to compare the results and to study the uniqueness/stability of the solution. DE optimization starts every time with a different random population of solutions, so running cyclotron mapping 10 times on the same data set provides a reasonable approximation of the stability of our solution. We found that

while there is some variability in the resulting cyclotron maps among the runs, the main emission features fortunately remain largely invariant.

### 3.2.1. Cyclotron Emission Regions

It appears that class 1 (Figure 16), which is mainly the low state of Sector 52, does not produce distinct cyclotron emission regions. The phasing and shape of the class 1 light curve suggest an ellipsoidal modulation as the likely origin,

**Table 3**  
AM Her Light-curve Classes

Class	Active Poles	Flux Level	$N$ Class Members	Remarks
1	none	low	104	ellipsoidal modulation
2	1+2 weak	low	101	ellipsoidal plus cyclotron
3	1	mid	36	rarely seen and shows a stream dip
4	1+2 weak	mid	284	mostly during the long slow descent toward the low state
5	2+3 weak	mid–high	215	most common in Sectors 14, 25, and 26
6	weak 2+3	high	180	high state, especially during flaring

consistent with our binary model fitting. This artifact results because the code spreads out the putative cyclotron emission all over the WD surface.

At other times, there is a northern pole at around longitude =  $10^\circ$ , latitude =  $+30^\circ$ . This location coincides with the pole in Schwöpe et al. (2020), where they see  $az = 12^\circ$  and colatitude =  $+65^\circ$  (latitude =  $+25^\circ$ ). This pole seems to dominate class 2 (Figure 17), class 3 (Figure 18), and class 4 (Figure 19) and is particularly dominant in class 3. Classes 4, 5 (Figure 20), and 6 (Figure 21) show a second pole at the equator on the far side of the WD. Classes 5 and 6 show a third (southern) pole at long. =  $+90^\circ$ – $100^\circ$ , lat. =  $-20^\circ$ . The southern pole becomes the dominant pole for class 6. It also seems, looking at the plot of classifications (Figure 15), that class 6 is associated with strong flaring episodes in the light curve. Intriguingly, Schwöpe et al. (2020) also discovered a second (far side from the donor) pole, active during periods of blobby accretion and flaring. We call the northern pole (long. =  $+10^\circ$ , lat. =  $+30^\circ$ ) pole 1, the equatorial pole at long. =  $+180^\circ$  pole 2, and the southern pole (long.  $+90^\circ$ – $100^\circ$ , lat.  $-20^\circ$ ) pole 3 and summarize our results in Table 3. We address the consequences of the presence of three accretion poles alternating in activity and their specific location in the discussion.

## 4. Discussion

### 4.1. Magnetic Field Structure

We derived a precise inclination for AM Her by modeling the low-state light curves from TESS. This allowed us to confidently model the high-state emission in order to locate accretion regions. The light curves usually show two well-localized spots at a time with a total of three separate spots visible at various times: a northern region (spot 1), an equatorial one (spot 2), and a southern one (spot 3). The northern and southern spots are rarely, if ever, seen at the same time. The equatorial spot 2 is often seen with either spot 1 or spot 3 rather than by itself. Based on the rough spot positions determined in the previous section, the angular distance between spots 1 and 2 is  $166^\circ$ , and there is  $90^\circ$  between spots 2 and 3. Spots 1 and 3 are not seen to be simultaneously active, but remarkably they are  $92^\circ$  apart on the stellar surface. Spots positioned orthogonally on the WD surface are a strong indicator of a multipolar (dipole plus quadrupole) magnetic field structure). One possibility is that spot 3 is located at the footpoints of one of the dipolar poles and spots 1 and 2 are each located  $90^\circ$  from the magnetic axis, hence on the magnetic equator. In this scenario, the angle between the rotational axis and the magnetic axis, i.e., the magnetic colatitude, is  $70^\circ$ . Accretion on or near the intersection of the orbital plane and the magnetic equator is expected theoretically in the case of multipolar magnetic accretion (Wickramasinghe & Wu 1991;

Wu & Wickramasinghe 1993; Wu & Mason 1996; Mason et al. 1998, 2022; Zhilkin et al. 2012, 2016). Shedding light on the complex magnetic field structure of the WD in AM Her accomplishes the second goal of this work. Next, we address the first goal.

### 4.2. High–Low States and Duty Cycles of Polars

One of the lessons that has been learned from decades of observations of the high and low states of polars is that the state behavior is system-dependent and is relatively stable over long timescales. While it is impossible to predict whether AM Her or AR UMa (recall Figure 1), with duty cycles of about 50% and 5% respectively, will be in a low state at a specific future time, those duty cycles and many other aspects of the long-term light curves are indistinguishable between light curves obtained decades apart (Livio & Pringle 1994; Wu & Kiss 2008). The same is also true for other polars (Duffy et al. 2022).

Observations indicate that the duty cycles of high–low states vary dramatically among polars (Ramsay et al. 2004; Mason & Santana 2015; Duffy et al. 2022). For instance, AM Her and AR UMa behave very differently, as seen in their 17 yr light curves shown in Figure 1. The complex dynamical behaviors of polars, such as those in AM Her, can be extremely persistent, and they might last over several decades (see, e.g., Wu & Kiss 2008). It is therefore useful to examine polars with contrasting distinguishable characteristics, so that we may gain an understanding of the mechanisms behind the complexity and diversity of the high–low states, the state transitions, and the variations of the duty cycles among polars.

The WDs in polars are known for their strong magnetic fields. More precisely, the WDs have a magnetic moment large enough to create a magnetosphere extending to reach the component star. A natural choice to start is therefore to assess how the WD magnetic field regulates the mass transfer process and interacts with the magnetic field of the component star. We therefore consider the system AM Her, which has a WD magnetic field of  $B \sim 13$  MG (Silber et al. 1996), as the fiducial reference, at the lower end of the WD magnetic field distribution. AR UMa, with  $B \sim 235$  MG (Schmidt et al. 1999), is chosen as the counterpart, as its WD has the highest known magnetic field in all polars.

### 4.3. Magnetic Interactions in Close Binaries

Polars are close binaries, along with RS CVn systems (see Uchida & Sakurai 1983; Karoff et al. 2016) and magnetic Algols (see Retter et al. 2005; Richards et al. 2012), that have unambiguous evidence of magnetic interactions between the two component stars (see, e.g., Campbell 1989; Li et al. 1994, 1995). In this respect, polars are clearly distinguishable from nonmagnetic CVs and the other mCV subclass, the

intermediate polars, which also have a highly magnetic WD. The magnetic interactions between the two stars lead to stellar magnetospheric and chromospheric activities, which are reflected in the flaring and quiescent emission in the radio (see, e.g., Lefevre et al. 1994; Umana et al. 1998; Toet et al. 2021) and X-ray bands (see, e.g., White et al. 1986; Lefevre et al. 1994; Franciosini & Chiuderi Drago 1995). These properties are clearly observed in RS CVn systems and some Algols. Polars are relatively latent in comparison (see Beasley et al. 1994; Barrett et al. 2017), although some polars (e.g., MQ Dra, Ramsay et al. 2021) do show optical flares, which are believed to be triggered by magnetic activities of the secondary star. Two common radiative processes associated with flaring radio emission from magnetic active stars are gyrosynchrotron and ECME (Mutel et al. 1998), and the same radio emission mechanisms also occur in polars (Barrett et al. 2017).

With this in mind, we now examine the subtle difference in the magnetic interactions between polars in cases where the WD has substantial influence and a marginal influence on the magnetospheric properties of the secondary star. In addition to the usual indicators of magnetospheric activities such as flaring radio emission that occur in RS CVn systems and magnetic Algols, magnetic transfer duty cycles provide an alternative measure, as the mass transfer in polars is regulated by the magnetic properties of the secondary star, regardless of whether the starspot model, the magnetic valve model, or the hybrid model is adopted (Duffy et al. 2022).

The essence of the magnetically regulated mass transfer scenario is based on the magnetohydrodynamic conditions near the L1 point. For polars, the magnetic field at the L1 point is determined jointly by the WD and the secondary star (see, e.g., Duffy et al. 2022; Mason et al. 2022, for this discussion). This is notably different than the mCV subclass of intermediate polars, where the secondary star is not influenced by the magnetic field of the WD. Note that the high-order magnetic field components drop off as  $B_n(r) \propto r^{-(2n+1)}$ , where  $n$  is the order of the magnetic field multipolar component. We may therefore ignore the quadrupole and higher-order components of the WD magnetic field and consider only the dipole component when accounting for the effect of the WD magnetic field at the L1 point. It can be shown that the dipole component of the WD magnetic field at the L1 point is

$$\begin{aligned} B_{\text{wd}}(r)|_{\text{L1}} &\approx \frac{\mathcal{Q}}{2} \frac{B_0 R_{\text{wd}}^3 (1+q)^2}{(1+(1+q)\Delta)^3} \left[ GM_{\text{wd}} \left( \frac{P_{\text{orb}}}{2\pi} \right)^2 \right]^{-1} \\ &\approx \frac{18 \mathcal{Q} (1+q)^2}{(1+(1+q)\Delta)^3} \left( \frac{B_0}{10 \text{ MG}} \right) \left( \frac{R_{\text{wd}}}{10^9 \text{ cm}} \right)^3 \\ &\quad \times \left( \frac{M_{\text{wd}}}{0.7 M_{\odot}} \right)^{-1} \left( \frac{P_{\text{orb}}}{3 \text{ hr}} \right)^{-2} \text{ G}, \end{aligned} \quad (1)$$

where  $B_0$  is the polar strength of the WD magnetic field,  $P_{\text{orb}}$  is the orbital period,  $R_{\text{wd}}$  is the WD radius,  $M_{\text{wd}}$  is the WD mass,  $q$  is the mass ratio (the mass of the secondary star normalized to the WD mass), and  $G$  is the gravitational constant. The geometrical factor  $\mathcal{Q}$  is of the order of unity. Its exact value depends on the orientation of the WD magnetic moments and the degree of offset of the magnetic moment components (see Wickramasinghe & Martin 1985; Wu & Wickramasinghe 1993) from the center of mass of the WD.<sup>14</sup> The correction factor  $\Delta$  is

<sup>14</sup> For the normalization used here, its value tends to larger than 1, as the system tends to minimize its magnetic interaction energy (Wu & Wickramasinghe 1993) and balance the magnetic torques (see Campbell 1989; Wickramasinghe & Wu 1991).

the displacement of the L1 point (normalized to the orbital separation) from the center of mass of the system.<sup>15</sup> For polars with orbital periods  $P_{\text{orb}} \sim 1.5\text{--}3$  hr,  $\Delta \sim 0.010\text{--}0.028$ .

For the binary AM Her,  $M_{\text{wd}} = 0.63 M_{\odot}$ ,  $M_2 = 0.289 M_{\odot}$ , and  $P_{\text{orb}} = 3.094$  hr. This gives  $\Delta = 0.01573$ . We consider the mass-radius relation from the empirical study of Parsons et al. (2017) and derive a radius  $R_{\text{wd}} \approx 8 \times 10^8$  cm for the WD in AM Her. If we adopt a polar field strength  $B_0 = 13$  MG (Silber et al. 1996) for the dipole component, then the WD magnetic field at the L1 point is about 23 G (for a conservative value  $\mathcal{Q} = 1$  adopted in Equation (1)). For AR UMa,  $M_{\text{wd}} = 1.125 M_{\odot}$ ,  $M_2 = 0.198 M_{\odot}$ , and  $P_{\text{orb}} = 1.923$  hr. This gives  $\Delta = 0.02544$ . The radius of a  $1.125 M_{\odot}$  WD is roughly  $R_{\text{wd}} \approx 5.5 \times 10^8$  cm. If we adopt a polar field strength  $B_0 = 230$  MG (Schmidt et al. 1996) then the WD magnetic field at the L1 point is about 142 G (for a conservative value  $\mathcal{Q} = 1$  adopted in Equation (1)).

#### 4.4. Magnetospheric Activity of the Secondary Star

Due to mass loss, donor stars will eventually become fully convective when their mass is lower than about  $0.35 M_{\odot}$  (see Chabrier & Baraffe 1997; Feiden et al. 2021; Käpylä 2021). The secondary stars in polars with orbital periods of 3.5 hr or shorter are therefore expected to be fully convective late M dwarfs. Low-mass M dwarfs are observed to exhibit various degrees of magnetism, and their polar magnetic field can range from about 100 G to several kG (Moutou et al. 2017). The magnetic fields of the cool M dwarfs are not often dominated by one or two lower-order components,<sup>16</sup> such as the dipole and the stretched quadrupole (see Yadav et al. 2015; Kochukhov 2021). Even for those with a surface field strength of several kG, the magnetic fields on most of the stellar surface would be well below the kG level, e.g., the magnetic field on  $>55\%$  of the surface of the M dwarf GJ644C is well below 1 kG, but it has an average surface field of  $\langle B \rangle = 2.6$  kG, which is contributed by some magnetic zones with a very strong localized field (reaching about 8 kG, see Shulyak et al. 2019). Supposing that the magnetic fields of the secondary in polars have properties not much different from those of the fully convective M dwarfs in the field, we would expect that they have a large fraction of their surface with relatively disordered magnetic fields with strengths below 1 kG, while a small fraction of the surface is covered by magnetic fields whose local strengths are several kG.

The WD magnetic field of AR UMa is at least comparable to, or even stronger than, the magnetic field on most parts of the secondary star's surface, although it is weaker than the most magnetic active regions, e.g., starspots, on the secondary star's surface. In contrast, the WD magnetic field of the system AM Her is substantially weaker than the most magnetic active regions on the secondary star's surface and may not match

<sup>15</sup>  $\Delta$  is the solution to the algebraic equation

$$\eta(\Delta - \eta)^2 - \lambda(\Delta + \lambda)^2 = \Delta(\Delta + \lambda)^2(\Delta - \eta)^2,$$

where  $\eta = (1+q)^{-1}$ ,  $\lambda = 1 - \eta$ , and  $q$  is the mass of the secondary star normalized to the mass of the WD (i.e., the mass ratio). This dimensionless equation determines the offset of the L1 point from the center of mass of the binary with unity orbital separation.

<sup>16</sup> Studies, e.g., Chabrier & Küker (2006), have shown that the operation of the  $\alpha^2\Omega$  dynamo in fully convective low-mass M dwarfs, in contrast with the  $\alpha\Omega$  dynamo in more massive stars, tends to show more high-order multipole characteristics, as the large-scale dipole field component and even quadrupole component can become unstable (see Rädler & Braeuer 1987; Hubbard et al. 2011).

those in the less magnetic active regions on the secondary star's surface. However, the resultant field may occasionally disrupt the flow at L1, causing short-lived low states, with the default state being the active one. It is now clear that in AR UMa the WD magnetic field can dominate at the L1 point when the starspots on the secondary star are far away. When the starspots move into the vicinity of the L1 point, the magnetic fields of the WD and the secondary would readjust to attain an energetically favorable configuration. In the system AM Her, the WD magnetic field cannot overwhelm the secondary star's magnetic field at the L1 point regardless of the locations of the starspots on the secondary star, and hence the main driver of the magnetism at the L1 point is the intrinsic migrations of starspots on the secondary star's surface.

#### 4.5. A Unified Mechanism for the High–Low States and State Transition for Polars

The high–low states and the state transitions had been attributed to the magnetic properties of the secondary stars, and early works include the starspot model proposed by Livio & Pringle (1994), in which the temporal cessation of mass transfer is caused by the migration of a starspot or a cluster of starspots to the L1 point. While the starspot model is appealing, it alone cannot satisfactorily explain the  $>50\%$  duty cycle of the high state in the polar AM Her. Thus, if assuming that the cessation of mass transfer is caused by a magnetically induced temporal blockage, the WD must play a role mechanically and/or magnetically (see Wu & Kiss 2008). Polars are synchronous or almost synchronous rotating binaries, and the synchronization is facilitated through the interaction of the WD magnetic field and the secondary star (see Chanmugam & Wagner 1977; Campbell 1989; Wu & Wickramasinghe 1993). As both the WD and the secondary star are magnetoactive, their fields must interact, and the interactions are determined by the relative orientation and strength of the WD magnetic field and the secondary star's local surface magnetic field in regions near the L1 point. The on-and-off mass transfer can now be explained in a natural manner, where the interaction can prohibit (blockage of mass flow) or facilitate (channeling of mass flow), depending on the magnetic configuration (see Duffy et al. 2022; Mason et al. 2022, for a detailed discussion on the interactive magnetic valve mechanism).

The question now needing an answer is: is the interactive magnetic valve specific for the system AM Her or is it a mechanism generally applicable to other polars, observed to undergo high–low states and state transitions but with different durations of the high–low state duty cycles? The study of Duffy et al. (2022) implicitly implies that the high state of AM Her is the default, with the in-and-out migration of the starspots, which interact with the WD magnetic fields, operating to restrain or to allow the mass outflow at the L1 point. It also points out that the presence of a small amount of ionized gas would be sufficient to allow the magnetic valve to operate, because the charged particles are a consequence of coronal activity and the neutral gas particles will collide with the charged particles trapped by the magnetic field. The WD magnetic field at the L1 point is not the primary driver in AM Her, rather it is the locations of the starspots on the secondary star's surface, because the WD magnetic field at L1 is weaker than the magnetic field on the secondary star's surface even for the less magnetic active regions, i.e., the starspot. The WD magnetic field, however, is an essential agent to facilitate the

starspots in the valve operation, which depends on the configuration of how the WD magnetic field lines and the secondary star's magnetic field lines are connected; see Mason et al. (2022) for this discussion in the context of the asynchronous polar BY Cam.

The situation in AR UMa is very different than that in AM Her. As shown above, the WD magnetic field of AR UMa at the L1 point is comparable to the field at the secondary star's surface, except for the most magnetoactive regions, i.e., the starspots. An immediate consequence is that the high state is no longer the default state, as the WD magnetic field has sufficient strength to disrupt the mass outflow regardless of the location of the starspots of the secondary star, provided that there are some charged particles near the L1 point. The occurrence of the high state is when the magnetic fields of the WD and of the secondary star cooperate to form a field configuration that allows mass to channel through the L1 point. This requires fine-tuning, as the mass transfer will be disrupted when either the WD field or the starspot field dominates at the L1 point. The direction of the field is also important. The magnetic field is roughly aligned with the WD spin axis, so the material leaving L1 experiences a barrier due to the WD magnetic field perpendicular to the stream motion, which acts like a magnetic valve; see Equation (3) in Mason et al. (2022). Thus, the default is the low state, where the subtle cooperation between the WD magnetic field and the secondary star's starspot magnetic field is absent. This scenario naturally explains the two key features of high–low states of AR UMa: (i) a small (5%) high-state duty cycle and (ii) the high states are not long-lasting, as shown in Figure 1. This is in contrast to the system AM Her, which can sustain long-lasting high states with about 50% high-state duty cycle for at least decades.

#### 4.6. Further Remarks

The scenario above for explaining the high–low state duty cycles and the state transitions of AR UMa is an extension of that for the system AM Her in Duffy et al. (2022) in the regime of a high WD magnetic field and small orbital separation. Note that the orbital evolution of compact stellar binaries, including CVs, with orbital periods of 2 hr or shorter is driven mainly by gravitational radiation (see, e.g., Verbunt & Zwaan 1981). For polars with strong magnetospheric interactions, the contribution of magnetic braking in driving the orbital evolution would be suppressed (see Li et al. 1994; Wickramasinghe & Wu 1994; Belloni et al. 2020). Thus, we expect that the mass transfer in AR UMa, which has a strongly magnetic WD, is driven almost solely by gravitational radiation. This in turn sets a well-defined constraint on the accretion luminosity of the system, at least theoretically. On the other hand, the observed X-ray luminosity, integrated over time across duty cycles, provides a measure of the empirical accretion luminosity.

Polars do not have an accretion disk, so the accretion luminosity of a polar is simply

$$L_{\text{acc}} \approx \left( \frac{GM_{\text{wd}}}{R_{\text{wd}}} \right) \frac{dM_2}{dt}, \quad (2)$$

where  $dM_2/dt$  is the rate of mass transfer from the secondary star to the magnetic WD. From Kepler's third law and the Roche-lobe filling condition of Paczyński (1971), it can be shown, for semidetached binaries with orbital evolution driven

by gravitational radiation alone, that

$$\frac{dM_2}{dt} \approx 1.2 \times 10^{-10} \left[ (1 + q)^{1/3} q^{2/3} (4 - 3q) \right]^{-1} M_\odot \text{ yr}^{-1}. \quad (3)$$

For AR UMa,  $M_{\text{wd}} = 1.125 M_\odot$  and  $R_{\text{wd}} \approx 5 \times 10^8$  cm, giving a mass transfer rate, equal to the WD mass accretion rate, of  $6.5 \times 10^{15}$  g s<sup>-1</sup> corresponding to an accretion luminosity of  $L_{\text{acc}} \approx 1.8 \times 10^{33}$  erg s<sup>-1</sup>.

Note that the accretion luminosity of polars can be decomposed into roughly three components:

$$L_{\text{acc}} = L_{\text{cyc}} + L_{\text{sx}} + L_{\text{hx}} = (\mathcal{R}_1 + \mathcal{R}_2 + 1) L_{\text{hx}}. \quad (4)$$

The subscripts ‘‘cyc,’’ ‘‘hx,’’ and ‘‘sx’’ in the expression above denote the optical/IR cyclotron radiation, the keV X-rays (presumably thermal bremsstrahlung radiation), and the soft X-rays, respectively, and  $\mathcal{R}_1 \equiv L_{\text{cyc}}/L_{\text{hx}}$  and  $\mathcal{R}_2 \equiv L_{\text{sx}}/L_{\text{hx}}$ . In the standard shock model for polars (see King & Lasota 1979; Lamb & Masters 1979; Wu 2000; Cropper et al. 2002), optical/IR cyclotron radiation and keV X-rays are from shock-heated plasma, and their luminosity ratio,  $\mathcal{R}_1$ , depends on the competition of cyclotron and bremsstrahlung cooling in the shock-heated region (see Imamura et al. 1987; Wu et al. 1994). Cyclotron cooling is expected to dominate over bremsstrahlung cooling for accretion poles with a strong magnetic field ( $\gg 10$  MG, see Lamb & Masters 1979; Wu et al. 1994). However, when the magnetic field is extremely high, reaching about 100 MG or higher, a standing shock would not be formed. Various scenarios were proposed for such accretion (see Kuijpers & Pringle 1982; Frank et al. 1988; Woelk & Beuermann 1996), and a common outcome is the depletion of hard X-rays, and UV and soft X-rays are emitted instead in the magnetically channeled accretion flow. Observations have shown many polars have strong soft X-ray emission with  $\mathcal{R}_2 > 10$  (see Ramsay et al. 2004; Mouchet et al. 2012), and some have values even approaching 1000 (V884, with  $\mathcal{R}_2 \sim 150$ –850, Ishida et al. 1998) or higher (V1309 Ori, with  $\mathcal{R}_2 > 6000$ , Schwarz et al. 2005).

AR UMa was observed in the X-ray bands in 1996. It was in a low state initially (with an optical  $V$  magnitude of about 16.1 in 1996 April) but entered a high state later (with an optical  $V$  magnitude reaching 15.0 in 1996 December). Its keV X-ray luminosity was  $L_{\text{hx}} \sim 1.8 \times 10^{29}$  erg s<sup>-1</sup> in the low state and  $\sim 10^{30}$  erg s<sup>-1</sup> in the high state, values derived from ASCA and RXTE observations respectively (Szkody et al. 1999). Taking the high-state duty cycle of AR UMa as 0.05 (see Figure 1), the keV X-ray luminosity averaged over the high- and low-state duty cycle is about  $2.2 \times 10^{29}$  erg s<sup>-1</sup>. The soft X-ray luminosity, assuming an absorbed blackbody spectrum, was derived to be  $> 2.5 \times 10^{32}$  erg s<sup>-1</sup> (Szkody et al. 1999) or  $3 \times 10^{33}$  erg s<sup>-1</sup> (Remillard et al. 1994), depending on the absorption column density. The derived value of  $L_{\text{acc}}$  above is consistent with the observed soft X-ray flux. In the magnetic valve scenario, the magnetic field of the WD in AR UMa is strong enough not only to produce a soft-hard X-ray luminosity function of  $\mathcal{R}_2 \equiv L_{\text{sx}}/L_{\text{hx}} \sim 1000$  but also to give rise to a default state that is the low state, with an occasional high state occupying only 5% of the duty cycle. The expected rate of mass transfer driven by orbital evolution is consistent with X-ray and UV observations.

Finally, given that the interactive valve mechanism appears to apply to AM Her, AR UMa, and very likely to other polars, we may address related systems such as the mCVs, called low accretion rate polars (LARPs) or pre-polars, which are two groups that are difficult to distinguish. These CVs typically contain WDs with 50–60 MG fields and M3V to M6V donors. While in both cases the donor star underfills its Roche lobe, the LARPs could be polars in deep low states controlled by the high WD magnetic field like AR UMa or be the progenitors of polars (pre-polars) about to fill their Roche lobes for the first time. In either case, the evolution is expected to be driven almost entirely by gravitational radiation because of donor wind accretion, which is described by the magnetic siphon model of Webbink & Wickramasinghe (2005). Since the WD magnetic field is sufficiently strong to dominate the energy density of the donor wind, the WD is expected to accrete almost the entire magnetized wind outflow of the detached donor. True LARPs may be those polars in magnetically inhibited low states that remained dormant for extended periods, only to occasionally transfer mass via Roche lobe overflow.

## 5. Conclusion

AM Her is the original and by far the best-studied member of the class of highest magnetic field cataclysmic variables known as polars. AM Her has an orbital period,  $P_{\text{orb}} = 3.09$  hr, just above the edge of the CV period gap. The white dwarf in AM Her has a magnetic field of 13 MG, which is at the lower end of the polar distribution. On the other hand, the WD in AR UMa has the highest magnetic field known in a magnetic cataclysmic variable (235 MG), and a shorter orbital period,  $P_{\text{orb}} = 1.93$  hr, at the lower end of the CV period gap. Consequently, their comparison offers an opportunity to examine the underlying physics. The existence of high and low brightness states, observed in the X-ray and optical, is found for most polars on timescales of months to years. We propose a magnetic valve operating at the inner Lagrangian point (L1) in polars. We apply this model to AM Her and AR UMa, which lie at extremes in the WD magnetic field at L1 by three orders of magnitude. The long-term variability between high and low states is governed by the WD magnetic field strength at L1.

Incidentally, the results of the present study allow for a test of the persistent radio emission model for AM Her and AR UMa. Suppose that the radio emission region(s) are reasonably well localized around L1. The binary inclination must be known to properly interpret the observed orbital modulation. From the binary modeling presented in this paper, we may conclude that the moderately inclined ( $i = 50^\circ$ ) AM Her should produce some reduction of radio flux at phase 0 as observed (Gawroński et al. 2018), while AR UMa (with  $i = 70^\circ$ ) should produce more modulation as a function of orbital phase, with a significant reduction in radio flux observed at orbital phase 0. However, the persistently detected radio emission may also depend on the accretion rate.

All CV donor stars should have strong magnetic fields because of saturation since stellar magnetic dynamos saturate for spin periods of less than 10 days. This should also be the case for fully convective stars that are expected to have  $\Omega^2$  dynamos. As K-band radio observations suggest (Barrett et al. 2017, 2020), the donor star can have magnetic fields of  $\sim 8$  kG. AR UMa is expected to have a lower accretion rate than AM Her because it is below the period gap and AM Her is above. However, the radio flux from AR UMa is usually stronger than




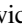

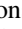
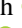


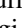



that of AM Her. The reason for the greater radio emission from AR UMa is likely that the donor star has fewer open field lines, i.e., more donor field lines are connected to the WD, and therefore most of the accretion occurs via a wind and not via the L1 point; whereas in AM Her most of the accretion occurs via L1, because its magnetic braking is greater and more of its field lines are open. So, the strength of the WD magnetic field has an effect on the high and low states. It is not just the L1 point that comes into play, but the entire magnetic field of the donor star. In essence, the WD will always be accreting from the donor star, because some fraction of its wind is constrained by the closed field lines of the WD and donor star. This is the low state. When the angular momentum loss is sufficiently high that the ram pressure at the L1 point becomes so great it overpowers the magnetic pressure, accretion occurs via the L1 point. This is the high state. The specific location of starspots on the donor star may not be too significant as they will contribute to the accretion as long as their field lines are connected to the WD.

### Acknowledgments

We thank the TESS Guest Investigator Program for providing 2 minute cadence observations of the binaries AM Her and AR UMa. We are also grateful to an anonymous referee for helpful comments and suggestions. We thank Claudia V. Rodrigues for helpful discussions concerning the binary modeling and for contributing Figure 2. P.A.M., L.C.M., and H.C.S. acknowledge support from Picture Rocks Observatory. P.S. and C.L. acknowledge support from NSF grant AST-1514737. P.G. and C.L. acknowledge support from NASA grants 80NSSC19K1704 and 80NSSC22K0183. G.R. and C.D. acknowledge Armagh Observatory & Planetarium, which is core funded by the Northern Ireland Executive. C.D. acknowledges support from UKRI grant (ST/T505936/1). K.I. was supported by Polish National Science Center grant Sonata 2021/40/C/ST9/00186. This work has made use of the NASA ADS and McDonald Observatory.

### ORCID iDs

Paul A. Mason  <https://orcid.org/0000-0002-5897-3038>  
 Kinwah Wu  <https://orcid.org/0000-0002-7568-8765>  
 Paul E. Barrett  <https://orcid.org/0000-0002-8456-1424>  
 Krystian Iłkiewicz  <https://orcid.org/0000-0002-4005-5095>  
 Colin Littlefield  <https://orcid.org/0000-0001-7746-5795>  
 Francisco Jablonski  <https://orcid.org/0000-0002-0386-2306>  
 Peter Garnavich  <https://orcid.org/0000-0003-4069-2817>  
 Paula Szkody  <https://orcid.org/0000-0003-4373-7777>  
 Gavin Ramsay  <https://orcid.org/0000-0001-8722-9710>  
 Christopher Duffy  <https://orcid.org/0000-0001-6662-0200>  
 Simone Scaringi  <https://orcid.org/0000-0001-5387-7189>

### References

- Araujo-Betancor, S., Gänsicke, B. T., Long, K. S., et al. 2005, *ApJ*, **622**, 589  
 Bai, Y., Justham, S., Liu, J., et al. 2016, *ApJ*, **828**, 39  
 Bailer-Jones, C. A. L., Rybizki, J., Fouesneau, M., Demleitner, M., & Andrae, R. 2021, *AJ*, **161**, 147  
 Bailey, J., Ferrario, L., & Wickramasinghe, D. T. 1991, *MNRAS*, **251**, 37P  
 Barrett, P., Dieck, C., Beasley, A. J., Mason, P. A., & Singh, K. P. 2020, *AdSpR*, **66**, 1226  
 Barrett, P. E., Dieck, C., Beasley, A. J., Singh, K. P., & Mason, P. A. 2017, *AJ*, **154**, 252  
 Bastian, T. S. 1987, PhD Thesis, Univ. Colorado  
 Beasley, A. J., Bastian, T. S., Ball, L., & Wu, K. 1994, *AJ*, **108**, 2207  
 Belloni, D., Schreiber, M. R., Pala, A. F., et al. 2020, *MNRAS*, **491**, 5717  
 Belloni, T., Psaltis, D., & van der Klis, M. 2002, *ApJ*, **572**, 392  
 Bond, H. E., & Tift, W. G. 1974, *PASP*, **86**, 981  
 Bookbinder, J. A., & Lamb, D. Q. 1987, *ApJL*, **323**, L131  
 Brainerd, J. J., & Lamb, D. Q. 1985, in *Cataclysmic Variables and Low-Mass X-ray Binaries*, ed. D. Q. Lamb & J. Patterson (Dordrecht: Reidel), 247  
 Campbell, C. G. 1989, *MNRAS*, **236**, 475  
 Chabrier, G., & Baraffe, I. 1997, *A&A*, **327**, 1039  
 Chabrier, G., & Küker, M. 2006, *A&A*, **446**, 1027  
 Chanmugam, G., & Dulk, G. A. 1982, *ApJL*, **255**, L107  
 Chanmugam, G., & Wagner, R. L. 1977, *ApJL*, **213**, L13  
 Chanmugam, G., & Wagner, R. L. 1978, *ApJ*, **222**, 641  
 Cowley, A. P., & Crampton, D. 1977, *ApJL*, **212**, L121  
 Cropper, M. 1990, *SSRv*, **54**, 195  
 Cropper, M., & Horne, K. 1994, *MNRAS*, **267**, 481  
 Cropper, M., Ramsay, G., Hellier, C., et al. 2002, *RSPTA*, **360**, 1951  
 Davey, S. C., & Smith, R. C. 1996, *MNRAS*, **280**, 481  
 Dobrotka, A., Negro, H., & Konopka, P. 2020, *A&A*, **641**, A55  
 Duffy, C., Ramsay, G., Steeghs, D., et al. 2021, *MNRAS*, **502**, 4953  
 Duffy, C., Ramsay, G., Wu, K., et al. 2022, *MNRAS*, **516**, 3144  
 Dulk, G. A., Bastian, T. S., & Chanmugam, G. 1983, *ApJ*, **273**, 249  
 Feiden, G. A., Skidmore, K., & Jao, W.-C. 2021, *ApJ*, **907**, 53  
 Ferrario, L., Wickramasinghe, D. T., & Schmidt, G. 2003, *MNRAS*, **338**, 340  
 Franciosini, E., & Chiuderi Drago, F. 1995, *A&A*, **297**, 535  
 Frank, J., King, A. R., & Lasota, J. P. 1988, *A&A*, **193**, 113  
 Gänsicke, B. T., Beuermann, K., & de Martino, D. 1995, *A&A*, **303**, 127  
 Gänsicke, B. T., Long, K. S., Barstow, M. A., & Hubeny, I. 2006, *ApJ*, **639**, 1039  
 Gänsicke, B. T., Schmidt, G. D., Jordan, S., & Szkody, P. 2001, *ApJ*, **555**, 380  
 Gawroński, M. P., Goździewski, K., Katarzyński, K., & Rycyk, G. 2018, *MNRAS*, **475**, 1399  
 Greenstein, J. L., Sargent, W. L. W., Boroson, T. A., & Boksteinberg, A. 1977, *ApJL*, **218**, L121  
 Hakala, P., Ramsay, G., Potter, S. B., et al. 2019, *MNRAS*, **486**, 2549  
 Harrison, T. E., Howell, S. B., Szkody, P., & Cordova, F. A. 2005, *ApJL*, **632**, L123  
 Hearn, D. R., & Richardson, J. A. 1977, *ApJL*, **213**, L115  
 Heise, J., Brinkman, A. C., Gronenschild, E., et al. 1985, *A&A*, **148**, L14  
 Howell, S. B., Gelino, D. M., & Harrison, T. E. 2001, *AJ*, **121**, 482  
 Hubbard, A., Rheinhardt, M., & Brandenburg, A. 2011, *A&A*, **535**, A48  
 Hudec, R., & Meinunger, L. 1976, *IBVS*, **1184**, 1  
 Iłkiewicz, K., Scaringi, S., Littlefield, C., & Mason, P. A. 2022, *MNRAS*, **516**, 5209  
 Imamura, J. N., Durisen, R. H., Lamb, D. Q., & Weast, G. J. 1987, *ApJ*, **313**, 298  
 Inight, K., Gänsicke, B. T., Blondel, D., et al. 2022, *MNRAS*, **510**, 3605  
 Ishida, M., Greiner, J., Remillard, R. A., & Motch, C. 1998, *A&A*, **336**, 200  
 Kafka, S., Honeycutt, R. K., Howell, S. B., & Harrison, T. E. 2005, *AJ*, **130**, 2852  
 Kalomeni, B. 2012, *MNRAS*, **422**, 1601  
 Käpylä, P. J. 2021, *A&A*, **651**, A66  
 Karoff, C., Knudsen, M. F., De Cat, P., et al. 2016, *NatCo*, **7**, 11058  
 King, A. R., & Lasota, J. P. 1979, *MNRAS*, **188**, 653  
 Knigge, C., Baraffe, I., & Patterson, J. 2011, *ApJS*, **194**, 28  
 Kochukhov, O. 2021, *A&ARv*, **29**, 1  
 Kohonen, T. 1990, *Proc. IEEE*, **78**, 1464  
 Kuijpers, J., & Pringle, J. E. 1982, *A&A*, **114**, L4  
 Lamb, D. Q., & Masters, A. R. 1979, *ApJL*, **234**, L117  
 Lefevre, E., Klein, K. L., & Lestrade, J. F. 1994, *A&A*, **283**, 483  
 Li, J., Wickramasinghe, D. T., & Wu, K. 1995, *MNRAS*, **276**, 255  
 Li, J. K., Wu, K. W., & Wickramasinghe, D. T. 1994, *MNRAS*, **268**, 61  
 Livio, M., & Pringle, J. E. 1994, *ApJ*, **427**, 956  
 Mähönen, P. H., & Hakala, P. J. 1995, *ApJL*, **452**, L77  
 Mason, P. A., Andronov, I. L., Borisov, N. V., & Chanmugam, G. 1994, in *ASP Conf. Ser. 56, Interacting Binary Stars*, ed. A. W. Shafter (San Francisco, CA: ASP), 346  
 Mason, P. A., Chanmugam, G., Raymond, J., et al. 1992, *IAU Circ.*, **5545**, 2  
 Mason, P. A., Fisher, P. L., & Chanmugam, G. 1996, *A&A*, **310**, 132  
 Mason, P. A., & Gray, C. L. 2007, *ApJ*, **660**, 662  
 Mason, P. A., Littlefield, C., Monroy, L. C., et al. 2022, *ApJ*, **938**, 142  
 Mason, P. A., Ramsay, G., Andronov, I., et al. 1998, *MNRAS*, **295**, 511  
 Mason, P. A., & Santana, J. B. 2015, *The Golden Age of Cataclysmic Variables and Related Objects—III (Golden2015) (Proceedings of Science)*, **16**  
 Mason, P. A., Wells, N. K., Motsoaledi, M., Szkody, P., & Gonzalez, E. 2019, *MNRAS*, **488**, 2881  
 Maze, T., Kieboom, K., & Heise, J. 1986, *MNRAS*, **221**, 513

- Miyamoto, S., Kimura, K., Kitamoto, S., Dotani, T., & Ebisawa, K. 1991, *ApJ*, **383**, 784
- Mouchet, M., Bonnet-Bidaud, J. M., & de Martino, D. 2012, *MmSAI*, **83**, 578
- Moutou, C., Hébrard, E. M., Morin, J., et al. 2017, *MNRAS*, **472**, 4563
- Mutel, R. L., Molnar, L. A., Waltman, E. B., & Ghigo, F. D. 1998, *ApJ*, **507**, 371
- Paczyński, B. 1971, *ARA&A*, **9**, 183
- Pala, A. F., Gänsicke, B. T., Belloni, D., et al. 2022, *MNRAS*, **510**, 6110
- Parsons, S. G., Gänsicke, B. T., Marsh, T. R., et al. 2017, *MNRAS*, **470**, 4473
- Pavelin, P. E., Spencer, R. E., & Davis, R. J. 1994, *MNRAS*, **269**, 779
- Potter, S. B., Hakala, P. J., & Cropper, M. 1998, *MNRAS*, **297**, 1261
- Priedhorsky, W. C. 1977, *ApJL*, **212**, L117
- Priedhorsky, W. C., & Krzeminski, W. 1978, *ApJ*, **219**, 597
- Rädler, K. H., & Braeuer, H. J. 1987, *AN*, **308**, 101
- Ramsay, G., Cropper, M., Wu, K., et al. 2004, *MNRAS*, **350**, 1373
- Ramsay, G., Hakala, P., & Wood, M. A. 2021, *MNRAS*, **504**, 4072
- Remillard, R. A., Schachter, J. F., Silber, A. D., & Slane, P. 1994, *ApJ*, **426**, 288
- Retter, A., Richards, M. T., & Wu, K. 2005, *ApJ*, **621**, 417
- Richards, M. T., Agafonov, M. I., & Sharova, O. I. 2012, *ApJ*, **760**, 8
- Ricker, G. R., Winn, J. N., Vanderspek, R., et al. 2015, *JATIS*, **1**, 014003
- Scaringi, S., Körding, E., Uttley, P., et al. 2012, *MNRAS*, **427**, 3396
- Schmidt, G. D., Hoard, D. W., Szkody, P., et al. 1999, *ApJ*, **525**, 407
- Schmidt, G. D., Szkody, P., Smith, P. S., et al. 1996, *ApJ*, **473**, 483
- Schwarz, R., Hedelt, P., Rau, A., Staude, A., & Schwöpe, A. D. 2002, in ASP Conf. Ser. 261, *The Physics of Cataclysmic Variables and Related Objects*, ed. B. T. Gänsicke, K. Beuermann, & K. Reinsch (San Francisco, CA: ASP), 167
- Schwarz, R., Reinsch, K., Beuermann, K., & Burwitz, V. 2005, *A&A*, **442**, 271
- Schwöpe, A. D., Worpel, H., Traulsen, I., & Sablowski, D. 2020, *A&A*, **642**, A134
- Shulyak, D., Reiners, A., Nagel, E., et al. 2019, *A&A*, **626**, A86
- Silber, A. D., Raymond, J. C., Mason, P. A., et al. 1996, *ApJ*, **460**, 939
- Šimon, V. 2016, *MNRAS*, **463**, 1342
- Stockman, H. S., Schmidt, G. D., Angel, J. R. P., et al. 1977, *ApJ*, **217**, 815
- Szkody, P., & Brownlee, D. E. 1977, *ApJL*, **212**, L113
- Szkody, P., Vennes, S., Schmidt, G. D., et al. 1999, *ApJ*, **520**, 841
- Tapia, S. 1977, *ApJL*, **212**, L125
- Tapia, S., & In, E. 1976, *IAU Circ.*, **2987**, 2
- Tapia, S., Stockman, H., & Angel, J. R. P. 1976, *IAU Circ.*, **2994**, 5
- Team, MAST 2021, *TESS Light Curves—All Sectors*, STScI/MAST, doi:10.17909/T9-NMC8-F686
- Toet, S. E. B., Vedantham, H. K., Callingham, J. R., et al. 2021, *A&A*, **654**, A21
- Uchida, S. E. B., & Sakurai, T. 1983, in Proc. of the Coll. 71, *Activity in Red-dwarf Stars*, ed. P. B. Byrne & M. Rodono (Dordrecht: Reidel), 629
- Umana, G., Trigilio, C., & Catalano, S. 1998, *A&A*, **329**, 1010
- Verbunt, F., & Zwaan, C. 1981, *A&A*, **100**, L7
- Watson, M. G. 1995, in ASP Conf. Ser. 85, *Magnetic Cataclysmic Variables*, ed. D. A. H. Buckley & B. Warner (San Francisco, CA: ASP), 179
- Webbink, R. F., & Wickramasinghe, D. T. 2005, in ASP Conf. Ser. 330, *The Astrophysics of Cataclysmic Variables and Related Objects*, ed. J. M. Hameury & J. P. Lasota (San Francisco, CA: ASP), 137
- White, N. E., Culhane, J. L., Parmar, A. N., et al. 1986, *ApJ*, **301**, 262
- Wickramasinghe, D. T., Bailey, J., Meggitt, S. M. A., et al. 1991, *MNRAS*, **251**, 28
- Wickramasinghe, D. T., & Martin, B. 1985, *MNRAS*, **212**, 353
- Wickramasinghe, D. T., & Meggitt, S. M. A. 1985, *MNRAS*, **214**, 605
- Wickramasinghe, D. T., & Wu, K. 1991, *MNRAS*, **253**, 11P
- Wickramasinghe, D. T., & Wu, K. 1994, *MNRAS*, **266**, L1
- Wilson, R. E., & Devinney, E. J. 1971, *ApJ*, **166**, 605
- Woelk, U., & Beuermann, K. 1996, *A&A*, **306**, 232
- Wright, A. E., Cropper, M., Stewart, R. T., Nelson, G. J., & Slee, O. B. 1988, *MNRAS*, **231**, 319
- Wu, K. 2000, *SSRv*, **93**, 611
- Wu, K., Chanmugam, G., & Shaviv, G. 1994, *ApJ*, **426**, 664
- Wu, K., & Kiss, L. L. 2008, *A&A*, **481**, 433
- Wu, K., & Mason, P. A. 1996, in Proc of the IAU Coll. 158, *Cataclysmic Variables and Related Objects*, ed. A. Evans & J. H. Wood (Dordrecht: Kluwer), 203
- Wu, K., & Wickramasinghe, D. T. 1993, *MNRAS*, **260**, 141
- Yadav, R. K., Christensen, U. R., Morin, J., et al. 2015, *ApJL*, **813**, L31
- Young, P., Schneider, D. P., & Shectman, S. A. 1981, *ApJ*, **245**, 1043
- Zhilkin, A. G., Bisikalo, D. V., & Mason, P. A. 2012, *ARep*, **56**, 257
- Zhilkin, A. G., Bisikalo, D. V., & Mason, P. A. 2016, in AIP Conf. Ser. 1714, *Space Plasma Physics* (Melville, NY: AIP), 020002